This is a repository copy of *Predictive SOLPS-ITER simulations to study the role of divertor magnetic geometry in detachment control in the MAST-U Super-X configuration*.

White Rose Research Online URL for this paper:
https://eprints.whiterose.ac.uk/id/eprint/203192/

Version: Published Version

Article:

PAPER • OPEN ACCESS

Predictive SOLPS-ITER simulations to study the role of divertor magnetic geometry in detachment control in the MAST-U Super-X configuration

To cite this article: O. Myatra *et al* 2023 *Nucl. Fusion* **63** 096018

View the article online for updates and enhancements.

Predictive SOLPS-ITER simulations to study the role of divertor magnetic geometry in detachment control in the MAST-U Super-X configuration

O. Myatra[1,2,*] ⓘ, **B. Lipschultz**[2] ⓘ, **D. Moulton**[1], **K. Verhaegh**[1] ⓘ, **B. Dudson**[3] ⓘ, **S. Orchard**[1,2], **A. Fil**[1] and **C. Cowley**[1,2]

[1] Culham Centre for Fusion Energy, Culham Science Centre, Abingdon OX14 3DB, United Kingdom of Great Britain and Northern Ireland
[2] York Plasma Institute, University of York, Heslington, York YO10 5DQ, United Kingdom of Great Britain and Northern Ireland
[3] Lawrence Livermore National Laboratory, 7000 East Avenue, Livermore, CA 94550, United States of America

E-mail: omkar.myatra@ukaea.uk

CrossMark

Abstract

The SOLPS-ITER code has been utilised to study the movement of the detachment front location from target towards the X-point for MAST-U Super-X plasmas. Two sets of detached steady state solutions are obtained by either varying the deuterium (D_2) fuelling rate or the nitrogen (N) seeding rate to scan the corresponding 'control' parameters of outboard midplane density, n_u, and the divertor impurity concentration, f_I. At seeding and fuelling rates $\sim 10\times$ and $\sim 5\times$ that required to start detachment at the divertor target, the detachment front only reaches $\sim 50\%$ of the poloidal distance to the X-point, l_{pol}, corresponding to a region of strong parallel gradients in the total magnetic field B. The region of strong total field gradients correlates with where the detachment front location becomes less sensitive to control parameter variation. This result is qualitatively consistent with the predictions of a simple, analytic detachment location sensitivity (DLS) model (Lipschultz *et al* 2016 *Nucl. Fusion* **56** 056007) which is based in a scaled parallel-to-B space, z. While the DLS model predictions are in agreement with SOLPS-ITER results in terms of where the front location becomes less sensitive to controls (i.e. in the region of strong parallel gradients in B), the DLS model predicts a higher sensitivity in the region of weak parallel gradients in B downstream as compared to the simulation results. Potential sources of differences between the SOLPS-ITER and DLS model predictions were explored: The DLS model does not include energy sinks beyond radiation from a single impurity nor cross-field energy transport. Momentum and particle balance are also not included in the DLS model. The tight opening into the divertor for flux surfaces could lead to variations in plasma-neutral pressure balance as the detachment front reaches that region, exactly how this affects the front movement needs further investigation.

---

* Author to whom any correspondence should be addressed.

(Some figures may appear in colour only in the online journal)

1. Introduction

An important challenge standing in the way of commercial fusion power is mitigating high heat and particle fluxes delivered to plasma facing components which form the surface of 'divertor targets' in tokamaks (e.g. [1, 2]). A phenomenon called 'divertor detachment' has been shown to lead to large reductions of plasma pressure at the target and concomitant drops in parallel heat and particle fluxes reaching the target [3–6]. The large parallel heat fluxes of a tokamak reactor will necessitate operation in the detached regime [7].

Detachment initiation requires low plasma temperature at the target (typically $\leqslant 5$ eV) [3] which is often achieved by increasing the outboard mid-plane density or introducing impurities which radiatively remove heat/energy from the divertor plasma [8–12], thus lowering the heat flux to, and electron temperature (T_e) at the target. Following detachment onset, a roughly uniform low plasma pressure and temperature region expands away from the target towards the X-point. The upstream end of that cold region is called the detachment front, which is contiguous to the low temperature edge of the 'thermal front' [13]—a region of steep temperature gradients driven by power losses (typically through radiation) from the flux tube in which the temperature transitions between the hotter upstream region and either the target (when attached) or the detachment front after detachment. The thermal front is often observed to move all the way to the X-point [6, 14, 15]. The presence of a low temperature region at the X-point can lead to varying degrees of core energy confinement degradation; either directly by introducing a cold region next to, or inside the separatrix; or indirectly, through easier penetration of neutrals and impurities across the separatrix. X-point radiation can also occur without much loss of energy confinement [16–18]. It is not clear why the impact of X-point radiation on core confinement varies so strongly across tokamaks.

The compression/enrichment of impurities and neutrals in the divertor has also been found to degrade during detachment, which can result in core contamination and also raises concerns for pumping helium in a reactor when the divertor is fully-detached [19, 20]. It is therefore important to identify the detachment front location that is optimal for both the divertor and the core plasma, and to find ways of holding it at that position; feedback control of the detachment front location is a requirement to hold the core-divertor system in an optimal state.

There have been a number of successful detachment feedback control experiments using impurity seeding gases for control of outer divertor detachment in H-mode plasmas [21, 22]. However, the detachment front was only held either at the X-point or at/near the target in those experiments. The ultimate goal is to determine if there is a core and divertor scenario that is compatible with a cost-effective, energy-producing,

controllable reactor, and that allows control of detachment to either hold a core-divertor solution constant or modify it as needs vary. Such reactor needs require the ability to hold the detachment front anywhere between the X-point and the target in order to study where the optimal front location is. The detachment front location depends on the divertor magnetic topology and on the values of the following 'control' parameters (not an exhaustive list): outboard midplane electron density, n_u, the divertor impurity density fraction, $f_I = n_z/n_e$ (where n_z is the impurity ion density and n_e is the electron density) and the power crossing the separatrix into the scrape-off layer, P_{SOL} [9, 10]. Holding the front at any location between target and X-point appears to be difficult in current devices due to a small 'detachment window'. The detachment window for a control parameter $C = n_u$, f_I or P_{SOL} is defined as the range $C_\times - C_t$ where $C_\times$ and C_t are values of C when the front is at the X-point and target respectively. A bigger detachment window corresponds to better control. An understanding of the dependence of the front location on control parameters is therefore crucial and is the subject of this study.

Both detachment control and detachment threshold have recently been addressed using an analytical model called, herein, the detachment location sensitivity (DLS) model which provides theoretical predictions of the detachment position dependence (as well as the detachment threshold) on the three control parameters discussed above and the divertor magnetic topology [23] (see also [24]). The model predicts that increasing connection length (poloidal flux expansion) and decreasing total magnetic field strength (total flux expansion) from X-point to target both decreases the detachment threshold and increases the detachment window for all control variables. In particular, the sensitivity of the detachment location along the magnetic field to controls is predicted to be inversely proportional to the gradient in the magnetic field strength (B) along the field line in the divertor. In other words, detachment location control is improved in regions of strong parallel B-field gradients which correspond to strong gradients in $q_{||}$. In the outer divertor, this means that the larger the parallel gradient in B (and therefore $q_{||}$), the larger the change in controls that is required to move the detachment front a given distance up that gradient and towards the X-point [23].

Alternative divertor configurations have been proposed which may enhance detachment control and power/particle exhaust through increased poloidal and total flux expansion. The Mega Amp Spherical Tokamak (MAST) has been upgraded to optimise the Super-X configuration [25–27], which will enable the largest total flux expansion in existing tokamaks (2.5–3× higher) as well as being tightly baffled to trap neutrals in the divertor. Thus, the MAST-U divertor provides a test bed to study detachment physics including detachment control and threshold. Those capabilities extend to comparisons of the Super-X to conventional as

well as other alternative divertor configurations in the same tokamak.

In this work, the SOLPS-ITER code package [28] has been used to perform two parameter scans to transition from attached (high-recycling), through the detachment threshold, to strongly detached conditions in the MAST-U Super-X geometry [29]. The primary focus of this work is on the role of parallel *B*-field gradients in detachment control, the core characteristic of the Super-X. The first detachment scan is performed at fixed input power, with the main ion fuelling rate varied (with no extrinsic impurities) to obtain a scan in the outboard midplane density, n_u. The second detachment scan, again at the same fixed input power, varies the divertor impurity fraction, f_I, by varying the nitrogen seeding rate at a fixed fuelling rate. In both the seeding and fuelling scans, we include a background level of carbon due to plasma sputtering the carbon first wall surfaces.

For each set of the steady state detached solutions obtained, the movement of various detachment location markers is tracked as a function of main ion and impurity injection rates. In both scans we observe a drop in the sensitivity of the detachment location to controls in a region of increasing parallel gradients in *B*. In the DLS model, only a linear variation in the divertor *B* field is considered, unlike what occurs in MAST-U. To address this limitation in the current application of the model, the DLS model is generalised to obtain predictions for arbitrary *B*-field variation in the divertor, and applied to the MAST-U Super-X geometry.

We find that the DLS model, in qualitative agreement with SOLPS results, predicts a significant reduction in sensitivity of the detachment location in parallel space to controls in a region of high parallel gradients in *B*. Said another way, the movement along a flux tube for a fixed increment in *N* seeding or D_2 fuelling decreases as the region of high parallel gradients in *B* is reached. Such slowing down of the detachment movement, if further substantiated, could provide a route to improved control of the detachment location. Ideally, further studies also lead to a divertor design where, without external input, the divertor plasma remains detached even when core plasma transients occur, including large increases in P_{SOL}. The research presented herein may help guide improvements in the DLS model which can then serve as a tool for future divertor design and optimisation. It should be noted that all quantitative plots in this work originate from SOLPS *predictive* simulations of MAST-U scans, some of which (e.g. nitrogen seeding) have not yet been performed in experiment.

This paper is organised as follows. The simulation setup and movement of some of the detachment front markers as a function of impurity seeding rate and main ion fuelling rate (the only input parameters varied in these scans) are both described in more detail in the following section. The DLS model is briefly described in section 3 and predictions are compared with the movement of detachment front markers in SOLPS. Some of the limits/caveats associated with comparing the predictions of this simplified model with SOLPS simulations are described in section 4. Conclusions and future directions are summarised in section 5.
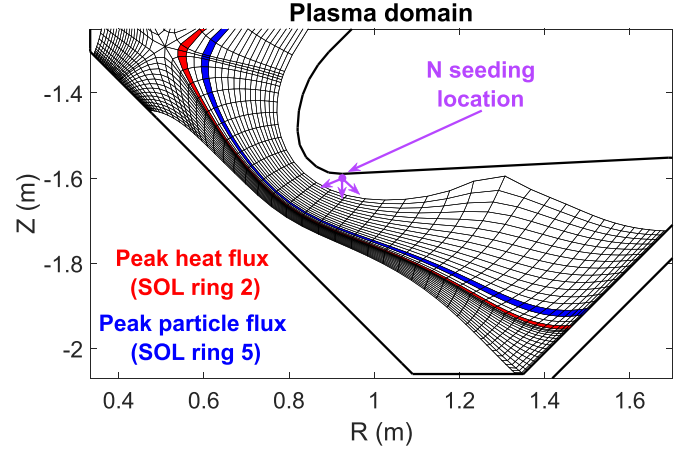

Figure 1. The divertor plasma simulation grid and nitrogen seeding location. Flux tubes that are chosen for this analysis are highlighted which correspond to the maximum heat (red) and particle flux (blue) to the target when the fuelling rate is $= 2 \times 10^{21} D$ nuclei s^{-1}.

2. SOLPS-ITER simulations of the MAST-U Super-X divertor

2.1. Simulation setup

As mentioned above, SOLPS-ITER is utilised in the studies described in this paper. Part of the connected double-null plasma simulation domain between the lower X-point and target is shown in figure 1, and it corresponds to Super-X divertor equilibrium similar to the ones used for previous MAST-U studies employing SOLPS [27, 29, 30]. In the analysis presented in further sections, we focus on the flux tubes that deliver the peak heat and particle fluxes to the target (in the attached phase), SOL rings 2 and 5 respectively, which are highlighted. In the fuelling scan, D_2 molecules are injected from the inboard midplane. The D_2 fuelling rate is varied from 1×10^{21} to 1.1×10^{22} D nuclei s^{-1}. For the impurity seeding scan, a case just before roll-over of the total particle flux to the target is chosen from the fuelling scan (fuelling rate $= 2 \times 10^{21}$ D nuclei s^{-1}), and nitrogen atoms are injected into the divertor near its entrance as shown in figure 1 (up-down symmetric). The nitrogen seeding rate is varied from 5×10^{19} to 1.1×10^{21} N s^{-1}. In each scan, steady state solutions are obtained for each fuelling or seeding rate.

Since this work is an extension of the predictive modelling presented in [27, 29, 30], we have used essentially the same physics model: the code was run with neutral-neutral collisions, impurity neutralisation and drifts turned off, and we do not solve for parallel currents in the SOL (no potential equation). The plasma boundary conditions and cross-field heat and particle diffusivities chosen in these simulations are identical to the ones presented in [29]. The total power entering the computational domain through the core inner boundary is 2.5 MW in each scan (split equally between ions and electrons), of which $\approx$2.1 MW goes to the low-field side and $\approx$0.4 MW goes to the high-field. In all cases, the cross-field heat diffusivity, $\chi_\perp = 10$ m^2 s^{-1} and particle

Table 1. EIRENE reactions included.

Database and reaction code	Reaction
AMJUEL H.4,10 2.1.5	$D + e \rightarrow D^+ + 2e$
AMJUEL H.4,10 2.6A0	$C + e \rightarrow C^+ + 2e$
AMJUEL H.4,10 2.7A0	$N + e \rightarrow N^+ + 2e$
AMJUEL H.4 2.2.9	$D_2 + e \rightarrow D_2^+ + 2e$
AMJUEL H.4 2.2.5g	$D_2 + e \rightarrow 2D + e$
AMJUEL H.4 2.2.10	$D_2 + e \rightarrow D + D^+ + 2e$
AMJUEL H.4 2.2.11	$D_2^+ + e \rightarrow 2D^+ + 2e$
AMJUEL H.4 2.2.12	$D_2^+ + e \rightarrow D + D^+ + e$
HYDHEL H.1,3 3.1.8	$D + D^+ \rightarrow D^+ + D$
METHANE H.1,3 3.2	$D^+ + C \rightarrow C^+ + D$
AMJUEL H.2 3.2.3	$D_2 + D^+ \rightarrow D + D_2^+$
AMJUEL H.0,1,3 0.3T	$D_2 + D^+ \rightarrow D_2 + D^+$
AMJUEL H.4,8 2.2.14	$D_2^+ + e \rightarrow D + D$
AMJUEL H.4,10 2.1.8	$D^+ + e \rightarrow D$
AMJUEL H.4,10 2.1.8	$D^+ + 2e \rightarrow D + e$

diffusivity, $D_\perp = 0.2 \text{ m}^2\text{s}^{-1}$ are used everywhere except in a small region near the separatrix in the core where, to emulate H-mode temperature and density pedestals, we have used $\chi_\perp = 2 \text{ m}^2\text{s}^{-1}$ and $D_\perp = 0.02 \text{ m}^2\text{s}^{-1}$. These diffusivities give radial SOL widths of $\lambda_q \approx 7.5$ mm and $\lambda_{n_e} = \lambda_{T_e} \approx 16$ mm, similar to values found in MAST H-mode experiments [31–33]. This value of λ_q is slightly higher than that predicted by the Eich scaling [34] for the 1 MA plasma current that this equilibrium is derived from, see [33] for more details. The radial resolution of our grid at the outboard mid-plane is such that we have 8 points between the separatrix and the first λ_q. Below the X-point (divertor SOLs and PFR regions), we set $D_\perp = \chi_\perp = 1 \text{ m}^2\text{s}^{-1}$.

The plasma-neutral interactions included in these simulations are shown in table 1. Nitrogen ionisation (AMJUEL H.4,10 2.7A0) is only included in the *N* seeding scan. Intrinsic carbon is included as a sputtered impurity in all scans, with 3% chemical sputtering yield as in previous MAST-U studies [27, 29].

2.2. Movement of detachment location in the poloidal plane

Detachment is typically accompanied by a variety of changes in the divertor plasma characteristics. In particular, there are plasma pressure losses due to volumetric momentum transfer from ions to neutrals at low ($T_e \leqslant 5$ eV) temperatures [3]. Thus in experiments, a target electron temperature of ≈ 5 eV is normally utilised as the threshold for detachment. In this work, we also use it as a marker to track the location of the front edge of the detached region. The $T_e = 5$ eV point can be tracked directly using the SOLPS output. Detachment also leads to movement of other measurable divertor characteristics. For example, various radiation profile peaks (hydrogenic, impurity or total) move towards the X-point as the extent of detachment from the target increases. Researchers have tracked the location of the point where the C-III radiation

drops to $1/e$ or 50% of the maximum towards the target [15, 35, 36], using that location as a rough proxy for the detached region's front edge (detachment location or front). In this spirit, we have tracked the locations at which the hydrogenic power losses (excitation plus ionisation, P_H) and power losses due to total impurity radiation (due to carbon in the fuelling scan, P_C; and both nitrogen and carbon in the seeding scan, P_{C+N}) drop to 50% of their maximum value along a flux tube on the target side of the peak. In addition, we have also tracked the locations at which these power losses peak. It should be noted here that in reality, the detachment front can be a rather nebulous thing and therefore difficult to strictly define. This is the reason why we choose to follow several definitions to see if they behave similarly. In the following, we discuss the movement of these markers as a function of the fuelling/ seeding rate.

In general, we find that the poloidal movement from target towards the X-point of the various markers tracked as a function of D_2 fuelling or N seeding rate slows down as their location approaches a region of high parallel gradient in B, which is also near the baffle or divertor entrance. The evolution of the $T_e = 5$ eV contours in the poloidal plane is shown in figures 2(*a*) and (*b*) for each detachment scan. The region in which the parallel gradient in B is greater than 50% of the maximum parallel gradient found across the *entire* divertor is shaded in grey. It can be seen that as the 5 eV contour approaches the region of high parallel gradients in B, the poloidal movement in the 2D plane becomes smaller than for the same increment in seeding or fuelling rate in a lower B gradient region. This drop in sensitivity of the $T_e = 5$ eV location to changes in the injection rate is seen in both scans. It should be noted that the definition used here to outline the grey region only serves as a rough indicator of where in the poloidal plane the parallel gradient B is relatively strong ($\geqslant 50\%$ of the maximum), and to illustrate the reduction in sensitivity of the 5 eV boundary to injection rates as it approaches this region. The difference between 'high' and 'low' parallel gradient in B is discussed in further detail in section 3.1.

A similar trend is observed in the movement of the hydrogenic and impurity power loss peaks. Figures 2(*c*)–(*e*) show the evolution of the poloidal profiles of T_e, P_H and P_{C+N} in SOL ring 5 from the seeding scan. We have chosen SOL ring 5 here because the power loss due to perpendicular transport only accounts for $\approx 10\%$–20% of the total in this flux tube, whereas this can be more than 50% in SOL ring 2 (more details in section 4.1). The evolution of the hydrogenic and impurity power loss profiles, however, is qualitatively similar in both SOL rings and in both scans. The movement of the P_H and P_{C+N} peaks, as well as the points at which P_H and P_{C+N} fall to 50% of maximum on the target side, are shown to also slow down for increasing seeding rate. Importantly, we find that the hydrogenic and impurity power loss peaks slow down around halfway in l_{pol} between the target and X-point. This is in contrast to what is typically observed in experiments—the radiating region typically moves to the X-point quickly after detachment onset. It is also interesting to note the relative
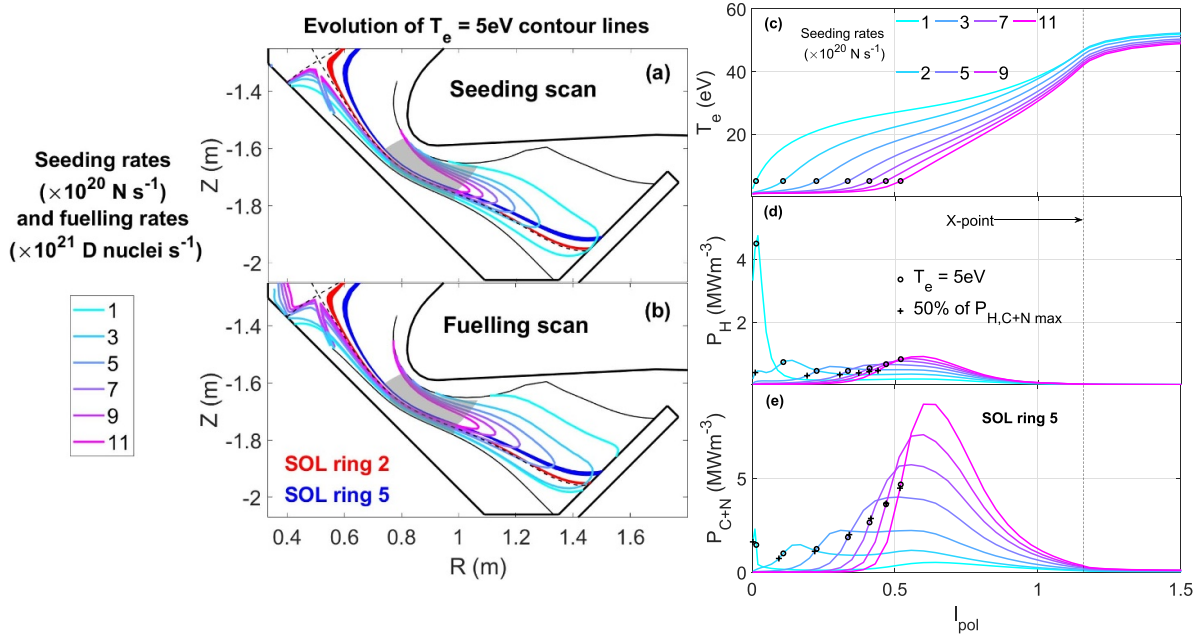
Figure 2. (*a*) and (*b*) Evolution of $T_e = 5$ eV contour lines during seeding and fuelling scans. The region in which the parallel gradient in B is greater than 50% of the maximum in the divertor is shaded in grey; (*c*)–(*e*): profiles of T_e, P_H and P_{C+N} are shown as a function of l_{pol} for the seeding scan to detachment. In addition, markers are added to denote the location of the $T_e = 5$ eV points (circles), as well as the location where P_H and P_{C+N} drop to 50% of maximum (crosses).

positions of the various possible detachment location markers along the P_H and P_{C+N} profiles in figures 2(*d*) and (*e*). The $T_e = 5$ eV point, which is difficult to track in experiment, typically lies close to 50% of the peak of the P_{C+N} and P_H profiles (side towards the target), which can be tracked in experiment.

The general reduction in sensitivity of the various potential detachment location markers introduced above to the injection rates is shown more clearly in figure 3, which displays their l_{pol} location as a function of seeding and fuelling rate for the SOL rings 2 and 5. The vertical dashed line shows the injection rate at which the 5 eV point leaves the target. In general, the 5 eV marker leaves the target shortly after the radiation peaks leave the near target region ($l_{pol} > 0$). The 5 eV markers are only a short distance downstream in l_{pol} from the radiation peaks for most injection rates. In both scans, locations of the 50% of $P_{H,max}$ and $P_{C,max}/P_{C+N,max}$ points leave the target shortly after the 5 eV point, but quickly 'catch up' and either coincide with the 5 eV point or are very close to it throughout most of the scan.

One of the changes in the divertor that is accompanied by the low temperatures is the significant reduction in the heat transported along the field by conduction. We find that the relative contribution of conduction to the parallel heat flux decreases in the detached region along a field line towards the target. In the Super-X case studied here, convection is the dominant heat transport mechanism in the detached region. Based on this, we also track the point where heat convection, q_{conv}, is equal to heat conduction, q_{cond}, shown in black in figure 3. It is interesting to see that this point also typically lies close to the $T_e = 5$ eV and 50% points on the radiation profiles throughout

both seeding and fuelling scans to detachment. This is similar to experimental observations in DIII-D where the parallel heat flux transported by convection was found to start dominating as T_e dropped below $\sim$10 eV [37]. In the DLS model, only the region between the midplane and the detachment front is treated, and convection is assumed to be negligible as typically done in simple SOL models. Further studies are needed, but for computational studies which have access to significantly more information on the plasma parameters compared to experiment, this additional detachment front marker where $q_{conv} = q_{cond}$ could serve as a physics based boundary marking the start of the detached region. It can be noted that this region where q_{conv} is the dominant heat transport mechanism is only localised below the X-point, and it does not seem to have an impact on the upstream conditions through both the scans.

The reader will note that the markers for the radiation peaks can abruptly move to larger l_{pol} for small changes in seeding or fuelling rates. This can be traced back to the profiles of radiation in figures 2(*d*) and (*e*): at low fuelling/seeding rates there can be two peaks in the profiles of P_{C+N} and P_H, one near the target, and the other upstream at $l_{pol} \approx 0.5 - 0.7$ m, in the region of high parallel gradients in B. As the injection rate is increased, the peak near the target drops and the peak upstream grows and thus the location of the higher peak changes abruptly from near the target to further towards the X-point. The drop in the peaks near the target most likely because the temperature there is dropping. The radiation loss parameter for both carbon and nitrogen strongly drops for temperatures below 5 eV; and transport effects tend to move the key radiators (C^{2+}, C^{3+}, N^{2+}, N^{3+}) to higher temperature regions
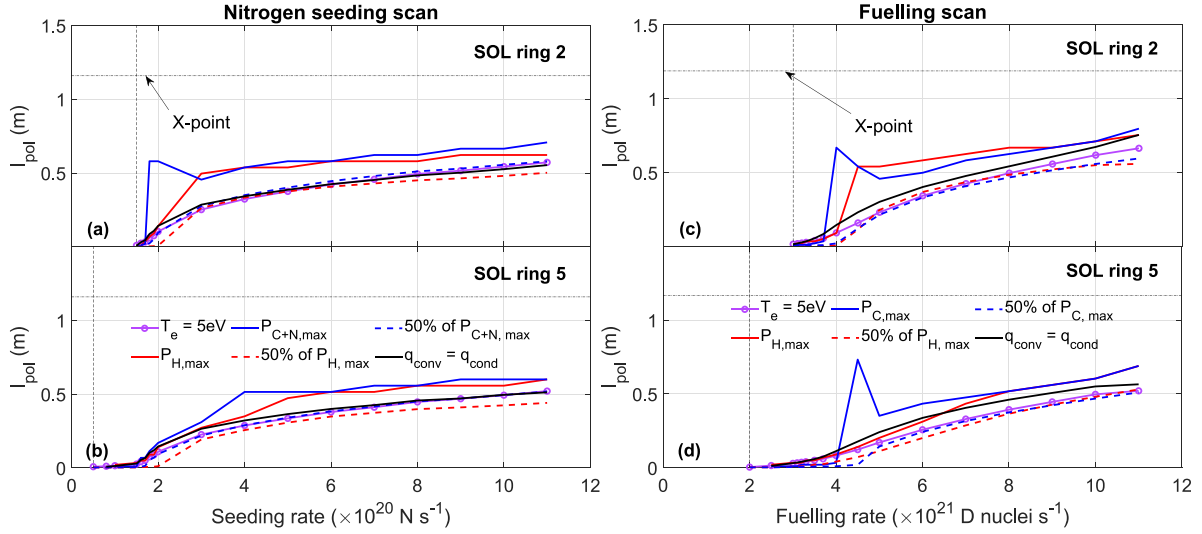
Figure 3. Poloidal distance, l_{pol}, from the target of the detachment front location markers for nitrogen seeding scan (*a*) and (*b*) as well as the D2 fuelling scan of the upstream density (*c*) and (*d*): 6 different 'markers' corresponding to the detachment front location are shown. See figures 2(*c*)–(*e*) for an illustration of the location of the various markers on the various profiles. The above results are shown for SOL ring 2 and SOL ring 5. The vertical dashed line shows the injection rate at which the 5 eV point leaves the target.
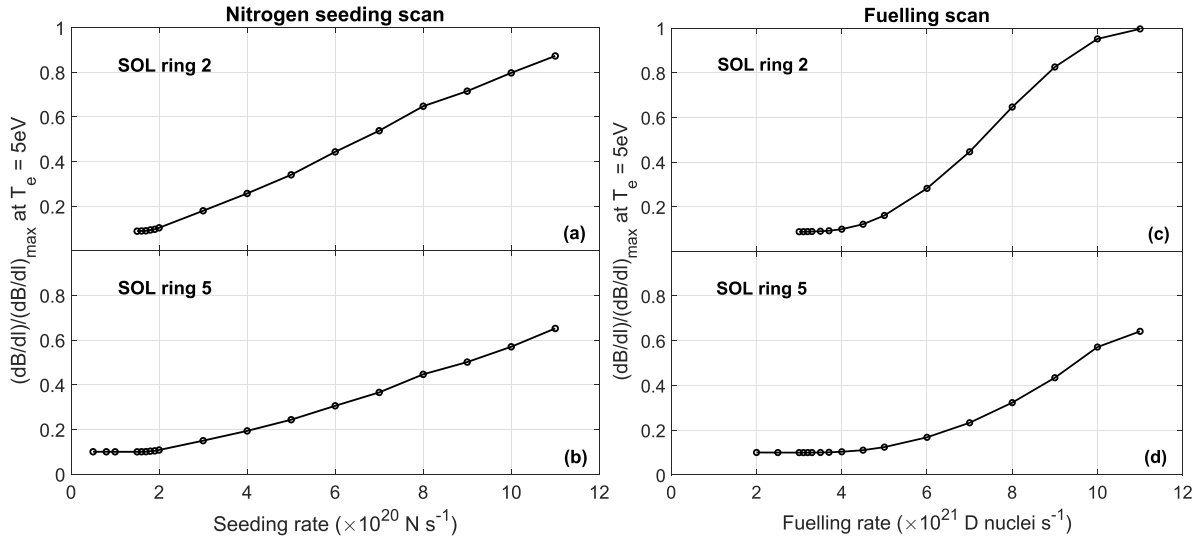

Figure 4. The parallel gradient in B, dB/dl, at the locations of the 5 eV point in SOL rings 2 and 5 as a function of N seeding and D_2 fuelling rate (normalised to the maximum value of dB/dl in those flux tubes).

[7]. Likewise, the effective hydrogenic cooling rate also drops significantly below 10 eV [38]. The target electron density and/or atomic density can still increase in this temperature range before the volume recombination and molecular effects become important, which could increase the radiative losses. However, the strong reduction in emissivity that is accompanied by the temperature falling below 5 eV appears to more than compensate for this effect in these cases.

Based on the above, the following markers are all useful for tracking the detachment front: the $T_e = 5$ eV point, the 50% point on the P_H and impurity radiation profiles (on the target side of the peak) and the point where $q_{conv} = q_{cond}$. However, for simplicity, we consider the flux tube to be 'detached' when

the 5 eV marker leaves the target when studying the movement of the detachment front.

As mentioned earlier, the sensitivity of the 5 eV boundary in figure 2 drops in a region of high parallel gradients in B. This is demonstrated in figure 4 which shows the parallel gradient in B, dB/dl, (where l is the parallel distance from the target) at each of the $T_e = 5$ eV locations in SOL rings 2 and 5 shown in figure 3, normalised to the maximum value of dB/dl in those flux tubes, as a function of seeding/fuelling rate. The fact that the movement of the 5 eV point in l_{pol} slows down as it moves through increasing dB/dl can be seen when studying figures 3 and 4 together: in the seeding scan (ring 2), the 5 eV point starts moving away from the target at

a seeding rate $\approx 1.5 \times 10^{20}$ N s^{-1}, and reaches $l_{\text{pol}} \approx 0.25$ m (figure 3) as the seeding rate is increased to 3×10^{20} N s^{-1}. Across this distance, dB/dl (figure 4) only increases from $\approx 10\%$ of the maximum to $\approx 15\%$–20%. However, to move the 5 eV point another 0.25 m upstream to $l_{\text{pol}} \approx 0.5$ m (figure 3), the seeding rate has to be increased from 3×10^{20} N s^{-1} to 11×10^{20} N s^{-1}; and across this distance, dB/dl (figure 4) increases significantly from $\approx 15\%$–20% of the maximum to $\approx 65\%$–85%. A similar trend is also observed in the fuelling scan.

In summary, a reduction in the sensitivity of the plasma profiles to impurity seeding and main ion fuelling rates is observed as increasing power loss occurs in a region of high parallel gradients in the magnetic field. In the next section, we study the movement of these points as a function of the 'physics' control parameters described in the DLS model—we will first briefly describe the key assumptions and model equations, and then compare predictions of the DLS model for MAST-U to the simulation results.

3. Comparison of DLS model and SOLPS-ITER predictions of detachment location

3.1. Modifications of the DLS model to apply to SOLPS data

Our modifications of the DLS model for this study are mandated by the need to apply the model to a situation where the variation of B along a field line is not linear; certainly true for the Super-X divertor. We follow the development of the DLS model for application to a single flux tube: power balance is used to predict the thermal/detachment front location as a function of n_{u}, which is taken to be the electron density at the outboard midplane; the impurity fraction, f_{I}, which is assumed to be constant in the flux tube and P_{div} which is the power passing through the flux tube at the X-point position.

The front moves along a mathematically convenient parallel co-ordinate z defined such that $z = 0$ at the target and $z = L$ at the outboard midplane. Note that the co-ordinate z is actually the volume of the flux tube between the target and z, scaled by a reference area ($\propto 1/B_\times$, $B_\times$ is the magnetic field strength at the X-point position). It is related to the actual parallel distance from the target (l) and poloidal distance (l_{pol}) as:

$$\text{d}z = \frac{B_\times}{B}\text{d}l = \frac{B_\times}{B_{\text{pol}}}\text{d}l_{\text{pol.}} \tag{1}$$

In other words, the element dz is essentially the actual elemental parallel distance dl scaled by the total flux expansion at that point in the divertor. As a result, the regions close to the target (where the total flux expansion is high) are elongated in z space compared to l space. This is illustrated in figures 5(a) and (b) which shows a comparison of z and l, and $B(z)$ and $B(l)$ for SOL ring 2. In the DLS model, the thermal front (within which the radiative power loss occurs) is assumed to be thin/small compared to $z_\times$ (the distance between the X-point and target in z); that assumption simplifies the calculation of the radiative loss as well as allowing the thermal front (and detachment location) to move a significant amount from $z = 0$ to $z = z_\times$.

It is useful at this stage to distinguish between the region of 'high' parallel gradients in B and the region of 'low' parallel gradients for a flux *tube*. The left y-axis of figure 5(b) shows the parallel profiles of B in z and l space. The right y-axis shows dB/dz normalised to the maximum dB/dz in that flux tube, $(\text{d}B/\text{d}z)_{\text{max}}$. It can be seen that the space between the X-point and target can be roughly separated into two distinct types of regions: one in which dB/dz is relatively low and one where it is relatively high, even though the transition between the low gradient region and the high gradient region is smooth. For simplicity, for the rest of this work, we define the region of 'high' gradients in a flux tube as the region where dB/dz is greater than 50% of the maximum between the X-point and the target (the 'FWHM' of the dB/dz profile). This has been illustrated in figure 5(b) for $B(z)$ where this region is shaded in grey. Although this definition is arbitrary, it serves as a useful indicator of where in z space dB/dz is relatively high for when we compare the DLS model predictions with SOLPS results.

The key difference between the DLS model and its application in this study is the treatment of the divertor magnetic field profile. The analytic DLS model assumes that B is a linear function of z. This simplifies the analytic calculations of the front location as a function of the control parameters. In the following we have generalized the DLS equations (in particular, equation 27 of [23]) to allow for any divertor magnetic field profile, and the integrals are evaluated numerically. The detachment front location z_f and the control parameters are related as follows:

$$\frac{n_{\text{u}}\sqrt{f_{\text{I}}}}{P_{\text{div}}^{5/7}} = \frac{1}{U}\frac{B(z_f)}{B_\times^{3/7}} \times \left[\int_{z_f}^{z_\times} B^2(z)\text{d}z + \int_{z_\times}^{L}\frac{B^2(z)(L-z)}{L-z_\times}\text{d}z\right]^{-2/7} \tag{2}$$

where U is assumed to be a constant related to the Lengyel integral [13, 23, 39–43]:

$$U = 7^{2/7}(2\kappa_0)^{3/14}\sqrt{\int T^{1/2}Q(T)\text{d}T} \tag{3}$$

where $Q(T)$ is the radiative loss parameter or 'cooling function' [44] and κ_0 is the electron heat conductivity coefficient.

There are other simplifications made in the analytic DLS model which make it difficult to properly compare DLS model predictions to SOLPS results. Two model assumptions which do not hold in the SOLPS case are (a) all the power entering the divertor is dissipated through radiation due to a single impurity species; and (b) that impurity fraction is constant in the flux tube. In SOLPS simulations, there are multiple radiating species (multiple impurities as well as hydrogen), and their concentrations are not constant along z. There are power loss mechanisms beyond radiation as well. To compare DLS model predictions with the MAST-U simulations presented here, we have utilized an 'effective power loss species fraction', f_{eff}, which is defined (see section 3.2) to account for power losses from multiple impurity species and also the main ion species; f_{eff} is used in place of the impurity concentration f_{I}. We note that while the gas injection rates are the only parameters varied in the simulations, all three control parameters of the model
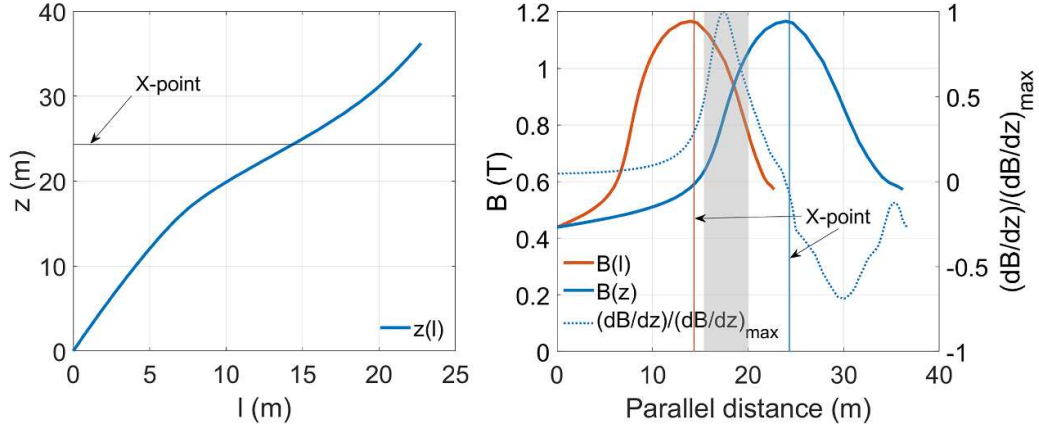
Figure 5. (*a*) The parallel coordinate *z* as a function of the actual parallel distance from the target (*l*), given for SOL ring 2. For this flux tube, *B* field between target and outboard midplane is shown on the left *y*-axis of figure (*b*) as a function of both *l* and *z*. d*B*/d*z*. The right *y*-axis of figure (*b*) shows d*B*/d*z* normalised to the maximum d*B*/d*z* in that flux tube as a function of *z*.
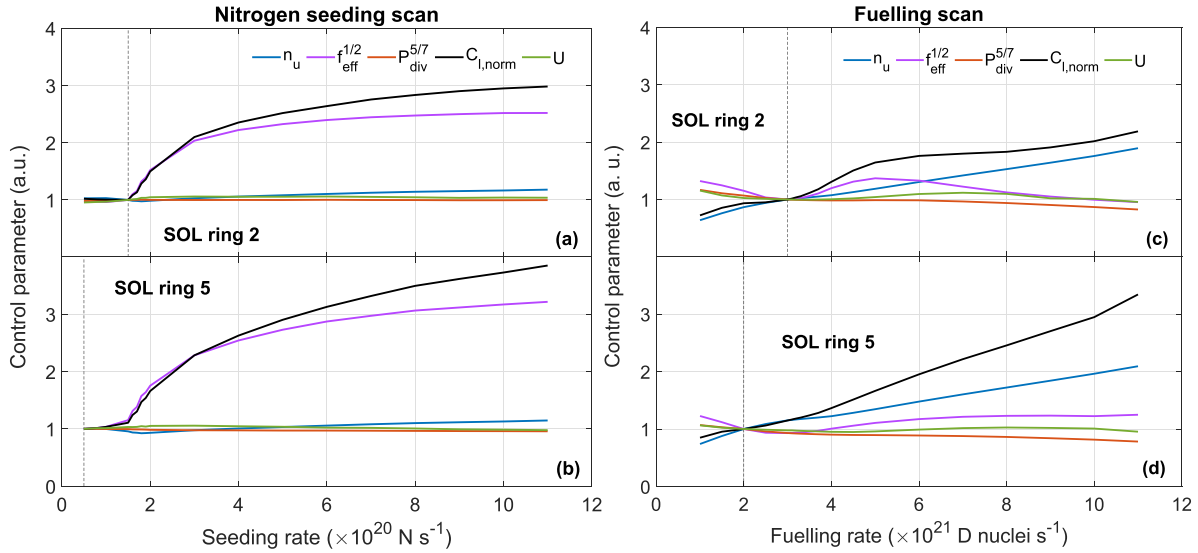

Figure 6. Variation in the normalised lumped control parameter, $C_{l,\mathrm{norm}}$ and its components (all normalised to their value when $T_e = 5$ eV leaves the target) shown as a function of seeding and fuelling rates for different scans as well as the 2 analysis rings, shown in figure 1. The seeding/fuelling rates at which the 5 eV point leaves the target (i.e. when $C_{l,\mathrm{norm}} = 1$) are marked with vertical lines.

are affected. Because of this we use a 'lumped' physics control parameter, C_l, which will include simultaneous change in n_u, f_{eff} and P_{div} as the gas injection rate changes:

$$C_l(z_f) \equiv \frac{n_u \sqrt{f_{\mathrm{eff}}}}{P_{\mathrm{div}}^{5/7}}. \tag{4}$$

In our comparison of the DLS model to the SOLPS calculations of detachment location movement, we are interested in comparing the DLS predictions of the *relative* changes in the control parameters. This is consistent with studies of other models using the Lengyel formulation [39] where the prediction of the divertor detachment threshold in f_I was over-predicted by factors $\geqslant 4$ [45, 46]. However, the relative trade-off between control variables in achieving detachment appeared to be accurate. Since we are interested in the relative changes in controls following detachment onset, we define a *normalised* lumped control parameter, $C_{l,\mathrm{norm}}$, and

take $C_l(z_f = 0)$ to be the value of C_l at the injection rate at which the 5 eV point is on the verge of detaching from the target:

$$
\begin{aligned}
C_{l,\mathrm{norm}}(z_f) &\equiv \frac{C_l(z_f > 0)}{C_l(z_f = 0)} \\
&= \frac{B_f \times \left[\int_{z_f}^{z_\times} B^2(z)\mathrm{d}z + \int_{z_\times}^{L} \frac{B^2(z)(L-z)}{L-z_\times}\mathrm{d}z \right]^{-2/7}}{B_t \times \left[\int_{z_t}^{z_\times} B^2(z)\mathrm{d}z + \int_{z_\times}^{L} \frac{B^2(z)(L-z)}{L-z_\times}\mathrm{d}z \right]^{-2/7}}.
\end{aligned}
\tag{5}
$$

Changes in $C_{l,\mathrm{norm}}$ and its components as a function of fuelling/seeding rate, relative to their value when the 5 eV point detaches, are shown in figure 6. The seeding/fuelling rates at which the 5 eV point leaves the target (i.e. when $C_{l,\mathrm{norm}} = 1$) are marked with vertical lines. We note that strictly speaking,

C_l and $C_{l,\mathrm{norm}}$ are only defined for the range $0 \leqslant z_f \leqslant L$ according to equations (4) and (5) respectively. In practice however, since the RHS of equation (4) will be finite even in attached conditions (i.e. when z_f is not defined or $T_e > 5$ eV at the target), we can still obtain values for $C_{l,\mathrm{norm}}$ when injection rates are below the threshold for $z_f \geqslant 0$. For completeness, we have also displayed $C_{l,\mathrm{norm}}$ and its components for injection rates below this threshold.

In the seeding scan, changes in $C_{l,\mathrm{norm}}$ are mainly driven by f_{eff} and there is little change in all other quantities. In the fuelling scan, while changes in $C_{l,\mathrm{norm}}$ are driven primarily by n_u, changes in f_{eff} are also significant. The assumed 'constant' U is also shown, and indeed there is little change in this quantity in both scans. Exactly how f_{eff} and U are defined and calculated from the SOLPS output is described in further detail in section 3.2. That is followed by a comparison of the modified DLS model predictions for MAST-U to the simulation results.

3.2. Extracting SOLPS equivalents of DLS model control variables

As mentioned earlier, given that the impurity fraction varies over the flux tube and the DLS model requires a constant fraction, we have developed f_{eff}, a constant along a flux tube. f_{eff} is defined to account for power losses from multiple species (impurity and hydrogenic), each with concentrations varying along the SOL. f_{eff} is defined using the same framework that the DLS analytical model uses to relate impurity levels and the corresponding power loss. To arrive at the expression for f_{eff} used in our analysis, we start from the DLS definition of a constant impurity (nitrogen) fraction in a flux tube, f_N (f_I is used in this paper if the impurity is not specified), generalize that so as to be applicable to a varying impurity concentration and then finally, to include the effect of power losses from hydrogen and carbon.

The DLS model defined the nitrogen concentration (f_N) as:

$$f_N = \frac{\sum_{i=0}^{Z^+} n_{N^i}}{n_e} = n_N/n_e \tag{6}$$

where Z is the atomic number of the impurity (in this case nitrogen) and n_N is the total nitrogen density (neutrals + ions). The nitrogen radiation power density, P_N, is then related to f_N through the radiation loss parameter which depends on the temperature, $Q_N(T)$. The resulting radiative power loss density is then

$$n_e n_N Q_N(T) = n_e^2 f_N Q_N(T) = P_N \ [\mathrm{Wm}^{-3}]. \tag{7}$$

In the case where f_N varies along the SOL, equation (7) can be integrated over the flux tube to give the total power radiated in the flux tube. The effective 'constant' nitrogen fraction required to dissipate the power that is radiated in that flux tube, $f_{\mathrm{eff},N}$, must then satisfy:

$$\int_{\mathrm{flux\ tube}} P_N dV = \int_{\mathrm{flux\ tube}} n_e^2 f_N Q_N dV = f_{\mathrm{eff},N} \int_{\mathrm{flux\ tube}} n_e^2 Q_N dV. \tag{8}$$

Therefore, $f_{\mathrm{eff},N}$ is defined as

$$f_{\mathrm{eff},N} \equiv \frac{\int_{\mathrm{flux\ tube}} P_N dV}{\int_{\mathrm{flux\ tube}} n_e^2 Q_N dV}. \tag{9}$$

All the quantities in the RHS of equation (9), including the radiative loss parameter for nitrogen, Q_N, can be obtained directly from the SOLPS output:

$$Q_N = \frac{P_N}{n_e n_N} \neq \sum_{i=0}^{Z^+} \frac{P_{N^i}}{n_e n_{N^i}} = \sum_{i=0}^{Z^+} Q_{N^i}. \tag{10}$$

Note that Q_N is not the sum of the cooling curves associated with each charge state, but more like an effective cooling curve for all the individual charge states of that species.

Having defined a logic that works for nitrogen, we turn our attention to allowing for additional species, e.g. carbon and/or deuterium. We determine an 'effective' constant radiating species fraction, f_{eff}, in a similar fashion to that shown for nitrogen:

$$f_{\mathrm{eff}} = \frac{\int_{\mathrm{flux\ tube}} [P_H + P_C + P_N] dV}{\int_{\mathrm{flux\ tube}} n_e^2 Q_{HCN} dV} \tag{11}$$

where

$$Q_{HCN} = \frac{P_C + P_N + P_H}{n_e(n_C + n_N + n_H)}. \tag{12}$$

In fact, Q_{HCN} defined as in equation (12) is used to calculate the constant U in the DLS model (equation (3)). Quantities on the RHS of equation (12) are obtained directly from the code and the integral in equation (3) is from the target to outboard midplane. With these definitions, in the case where f_N, f_C and f_H are constant, we recover $f_{\mathrm{eff}} = f_N + f_C + f_H$. Therefore, to account for losses from both the main ion species and multiple impurity species, the comparison is carried out by setting f_I in equation (2) to f_{eff}.

We can check which radiating species dominate changes in f_{eff} for each scan by comparing the effective fraction of each of the individual species. This is shown in figure 7. As expected, $f_{\mathrm{eff},N}$ is the dominant contribution to f_{eff} in the nitrogen seeding scan. However in the fuelling scan, changes in f_{eff} are driven mainly by $f_{\mathrm{eff},C}$ rather than $f_{\mathrm{eff},H}$; $f_{\mathrm{eff},H}$ does not change significantly through the scan. It should be noted that figure 7 does not show a decomposition of f_{eff}. Since the species fractions vary along the flux tube, f_{eff} is not the exact sum of the various fractions (which is also shown in the figure).

To summarize the above analysis: to account for the power losses from both the main ion species and multiple impurity species, the comparison between SOLPS and DLS is carried out by setting f_I in equation (5) to f_{eff}. The effect of line radiation power losses from both C and N as well as the deuterium ionization and excitation costs are accounted for through the effective radiating species fraction. However, that formulation does not generally raise the power loss accounted for substantially but does improve agreement with the DLS model predictions.
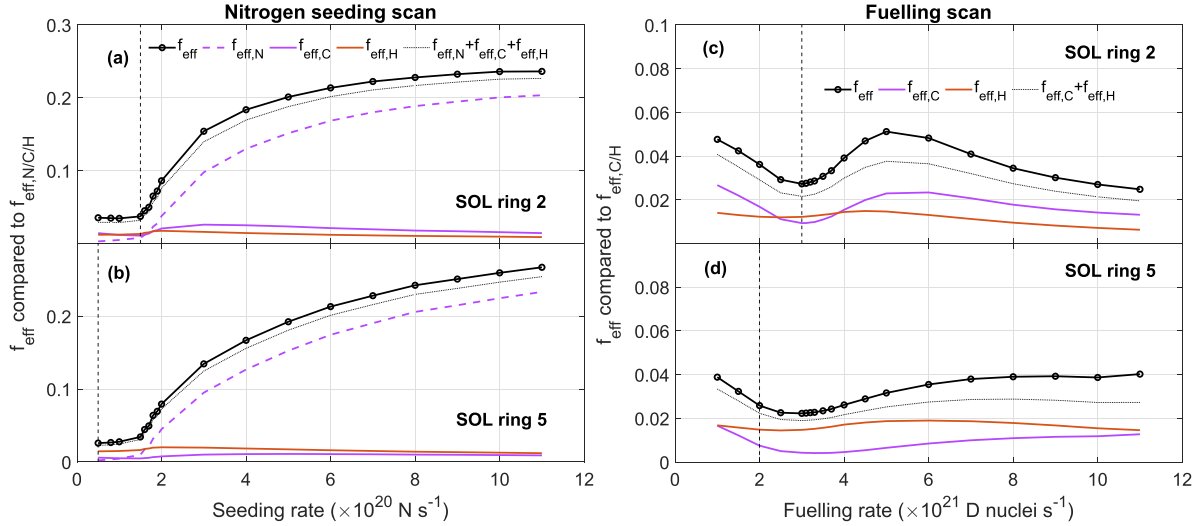
Figure 7. Evolution of f_{eff} compared to the individual effective radiating species fraction ($f_{eff,s}$ where $s = N, C, H$) and the corresponding sum.

It seems likely that in future high power devices, ITER and beyond, where the power crossing into the SOL, P_{SOL}, is strongly increased over current tokamaks and the SOL parallel heat flux width, λ_q, may remain similar, the parallel power flow towards the divertor, $q_{||} \propto P_{SOL}/\lambda_q$, will also be strongly increased. Such large $q_{||}$ would require increased impurity radiation compared to today's tokamaks in order to dissipate an overwhelmingly large fraction of the power entering the divertor.

Another DLS model parameter, κ_0, must also be abstracted from the SOLPS output. κ_0 is related to a scaled form of parallel heat flux $q = q_{||}B_\times/B$ (where $q_{||}$ is the parallel heat flux density) as follows:

$$\kappa_0 = \frac{qB^2}{T_e^{5/2}B_\times^2 \frac{dT_e}{dz}}. \tag{13}$$

Note that in our calculation of κ_0 from SOLPS output for use with the DLS model, equation (13), we only apply it to the part of the flux tube where the total parallel conducted heat is ten times larger than the total parallel convected heat. Then, the average of the resulting range of κ_0 values calculated is taken to be the value of κ_0 in equation (equation (3)) when calculating U. We find that κ_0 calculated from the SOLPS output and used to calculate U varies between ~1120–2190 in the fuelling scan and between ~950–1240 in the seeding scan. This variation in the conductivity is because of the application of flux limiters to the classical parallel conducted heat flux. However, due to the weak dependency of U on κ_0, the variation in U across both scans is small. The effect of accounting for convection in the DLS model on the detachment threshold (but not detachment window) has been studied in more detail in [24]. As it turns out, at least the detachment *threshold* predictions do not change significantly when convection effects are taken into account, so it is plausible that the effect on the detachment window is also relatively small.

3.3. DLS model and SOLPS-ITER predictions of front movement

The DLS model prediction of $C_{l,norm}$ for a given z_f is obtained by evaluating the RHS of equation (5) for the range $z_f = 0$ to $z_f = z_\times$. This is displayed by the solid black curve in figure 8. The z_f and $C_{l,norm}$ pairs derived from SOLPS output at each modelling D_2 and N injection rate once the 5 eV point leaves the target (LHS of equation (5)) are also shown, thus providing the various detachment position markers in z as a function of $C_{l,norm}$ for comparison with the DLS model. The peak in the impurity radiation losses is not shown because it generally coincides with the peak in the hydrogenic losses for most injections rates (figure 3).

Our application of the generalised ('non-linear') DLS model predicts for the four cases shown, that the detachment location should move quickly to the edge of the high dB/dz region (shaded in grey) and then strongly slow down as a function of increasing $C_{l,norm}$. We find that the SOLPS simulations also point to a general reduction in sensitivity of the location of the various detachment front markers to changes in $C_{l,norm}$ for all cases; the slowing down of movement is much reduced compared to the DLS model predictions. Let us first consider the movement between the target and $z = 10$ m. In this region, the movement is not as 'fast' as predicted by the generalised DLS model for any detachment front marker. Let us now consider the region beyond $z = 10$ m. In all cases, the movement of the SOLPS-derived $P_{H,max}$ marker (also the $P_{C,max}$ and $P_{C+N,max}$ markers, not shown) slows down significantly at the edge of the high dB/dz region, in qualitative agreement with the generalised DLS model. In the D_2 fuelling scan, the movement of the $T_e = 5$ eV location as well as of the markers corresponding to 50% of $P_{H,max}$ and $P_{C+N,max}$ also slow significantly at the edge of the high dB/dz region in both SOL rings. However, this is not clearly observed in the N seeding scan: only the $P_{H,max}$ marker slows down significantly at the
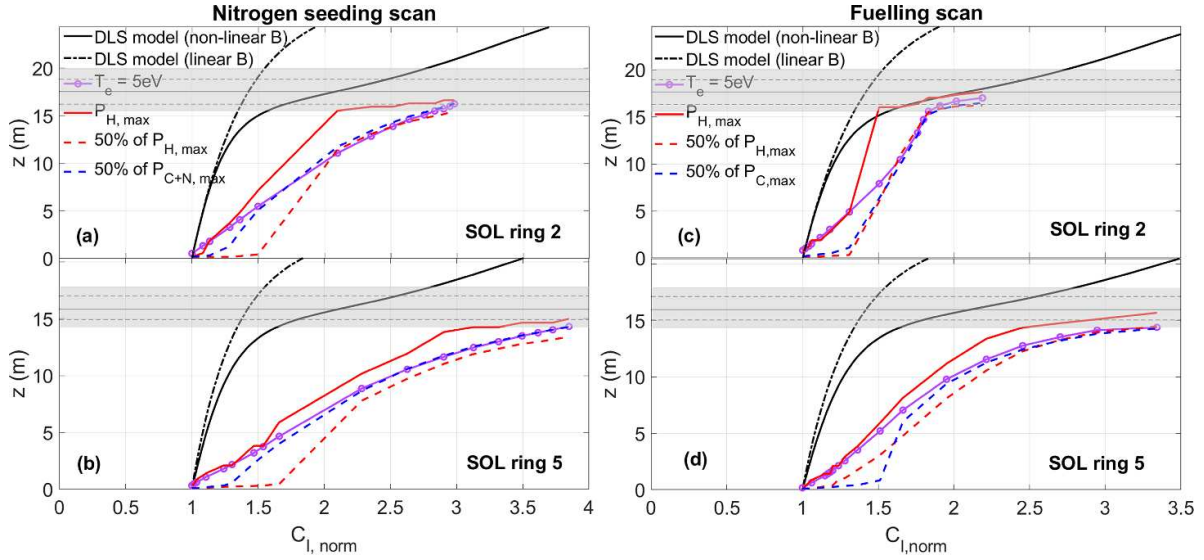
Figure 8. Predictions of the detachment front location, z_f, obtained from the generalised (solid black) and linear (dot–dash black) DLS models are shown as a function of $C_{l,\text{norm}}$. The markers of the detachment location determined from SOLPS are also shown. The region in which $dB/dz > 50\%$ of max dB/dz in that flux tube is shaded in grey, and the peak and 75% B gradients are marked with the solid and dashed horizontal lines respectively.

edge of the high dB/dz region in both SOL rings, but this does not appear as significant for the markers in the N seeding scan.

We note that the 5 eV point and the 50% points tracked in SOLPS (which we refer to as the detachment front location) also represent the cold end of the *thermal front* which sits between the detachment front and the X-point. Therefore, it is likely that most of the *thermal front* is actually in the high dB/dz region in both the flux tubes by the end of both scans.

It is interesting to note the relative position of the various SOLPS markers, markers corresponding to 50% of $P_{H,\text{max}}$ and $P_{C+N,\text{max}}$, lag behind the $T_e \approx 5$ eV location when the detachment front is near the target, and all three markers become closer to the $P_{H,\text{max}}$ marker towards the end of the scan. Since the $P_{H,\text{max}}$ marker is almost always upstream of these three markers, this loosely points to a variation in the width of the thermal front through the both the scans. More generally, it highlights an important difference between the SOLPS results and the DLS model assumptions: the SOLPS results indicate that the thermal front likely has a finite width in these simulations which can vary significantly as it moves upstream, whereas the DLS model assumes that the thermal front width is small enough that the hot and cold ends of the thermal front are effectively at the same location.

Also plotted in figure 8 is the DLS model prediction assuming linear variation in B between the X-point and target (black dash-dot line), with a dB/dz similar to that in the 'low' dB/dz region of our SOLPS simulation (z between 0–10 m, see figure A.13), and effectively a $B_\times/B_t$ similar to that in a conventional divertor. This 'linear' DLS model predicts a detachment front location sensitivity that is similar to that in 'low' dB/dz region of the non-linear (real B-field) case, but the significant reduction in this sensitivity predicted in the non-linear case is not predicted in the linear case. The linear DLS prediction does show a slight reduction in the sensitivity of z_f to

$C_{l,\text{norm}}$ as the front moves towards the X-point (this is due to the connection length being reduced as opposed to any field affect as described in [23, 24]), but this 'slowing' is much less strong compared to the real B-field case. This is primarily due to a high $B_\times/B_t$, discussed further in appendix.

To summarise, the analytical DLS model appears to qualitatively capture an important trend observed (less strongly) in both the SOLPS scans, i.e. the reduction in the sensitivity of the detachment front location to controls as the front moves through a region of increasing parallel gradient in the total magnetic field. This reduction in sensitivity predicted by the DLS model is essentially driven by the strong dB/dz itself. However, the SOLPS markers we track do not move as 'fast' as predicted by the generalised DLS model between the target and $z = 10$ m. This is could be due to the additional physics in the SOLPS model that is not captured in the DLS model. Potential reasons for the lack of a quantitative agreement and differences between the physics included in the DLS model and SOLPS will be discussed in the next section.

4. Discussion

In section 3 we have described the qualitative agreement between the DLS model and SOLPS simulations. As described in [23], the physics underlying the DLS model is related to the reduction in the parallel heat flux density through impurity radiation as well as due to the reduction of B along the field line. In other words, a larger parallel heat flux density must be dissipated as the thermal front moves upstream, requiring a bigger change in the control parameters to move the front up the flux tube in regions where the B field is increasing in the direction of movement. This is could be a reason why we see a qualitative agreement between the DLS model and simulation results since this physics would also be captured in SOLPS.
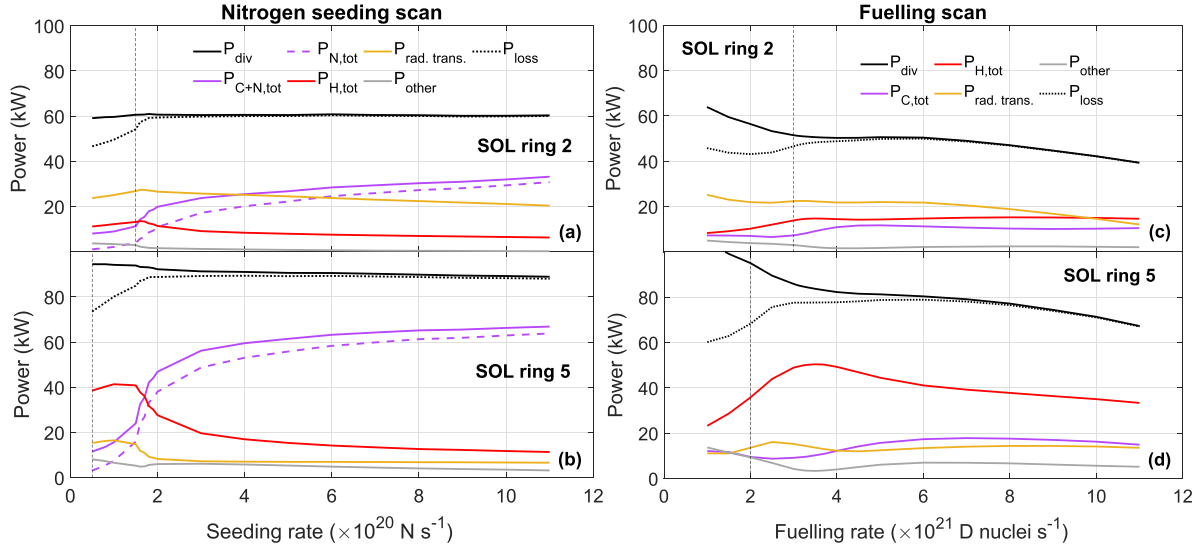
Figure 9. Description of contributors to power balance as a function of (*a*), (*b*) nitrogen seeding rate; and (*c*), (*d*) D_2 fuelling rate. Shown are the total power entering the flux tubes at the 'X-point' position, P_{div}; the total power dissipated between X-point and target, P_{loss}; and the components of P_{loss} (RHS of equation (14)). The injection rate at which the 5 eV point leaves the target is marked with a vertical dashed line.

Such a slowing down of the detachment front has also been postulated [47] for X-divertor configurations which have strong poloidal flaring of the field near the divertor target. We note that the analysis in [47] attributes the slowing down of the detachment front location to the reduction in the neutral interaction area due to poloidal flux expansion, whereas the DLS model points to an increase in $q_{||}$ (moving upstream) due to total flux expansion. If the poloidal field in the divertor volume (between the X-point and target) of an X-divertor scenario were comparable to the toroidal field, and much weaker towards the target, it can be argued that both effects could fundamentally point to the same physics: both having a significant increase in the total magnetic field, so a higher $q_{||}$ must be dissipated by any given energy loss mechanism; by impurities in the case of the DLS model and by neutrals as in the qualitative analysis in [47]. Further work is required to assess this potential connection.

Based on the simplifying assumptions of the DLS model and the approximations of DLS parameters from the SOLPS predictions, we do not expect quantitative agreement between the two predictions presented here. Another important difference between the DLS and SOLPS predictions is the additional physics accounted for in SOLPS (e.g. more kinds of power losses, impurity concentration varying, pressure loss). In this work, the emphasis is that the DLS model can potentially tell us *where* and *why* we can expect a reduction in the thermal front location sensitivity to controls. With this in mind, in the following we will discuss some of the specific differences between the DLS model assumptions and the SOLPS simulations, and possible reasons why a quantitative agreement with SOLPS simulations is not observed. In addition, movement of the detachment front in the poloidal plane (as opposed to *z*) and the potential role the baffle could play on the front location sensitivity is also discussed.

4.1. Differences between energy loss mechanisms included in the DLS model and SOLPS

It is clear from section 3 that the DLS model, for simplicity and ease of obtaining an analytic solution, ignores power loss mechanisms other than radiation from a single impurity that has a fixed concentration along the flux tube. This is also true of other analytic models that rely on the Lengyel formulation [39]. In SOLPS, multiple processes that remove power from a flux tube are present. The total power dissipated between X-point and target, P_{loss}, is given by equation (14):

$$P_{loss} = P_{C,tot} + P_{N,tot} + P_{H,tot} + P_{rad.\ trans.} + P_{other} \qquad (14)$$

The variations of each of the terms in equation (14) are shown as a function of injection rate in figure 9 for both the *N* seeding and D_2 fuelling scans. In the seeding scan, while total radiation due to carbon and nitrogen impurities ($P_{C,tot} + P_{N,tot}$) is the dominant power sink over much of the scan (mainly driven by nitrogen as one would expect), hydrogenic losses dominate over impurity radiation at low seeding rates. This makes sense as the seeding scan is started with a case from the fuelling scan that is at the edge of detaching. In the fuelling scan, the hydrogenic power losses (deuterium excitation and ionisation, $P_{H,tot}$) are significant and higher than losses due to carbon impurity radiation ($P_{C,tot}$) which only accounts for 10%–20% of the losses in both flux tubes, although both are comparable in SOL ring 2. Radiative and hydrogenic power losses together do not account for much more than half of the flux tube losses for SOL ring 2 in both detachment scans. Power losses due to radial transport ($P_{rad.\ trans.}$) dominate in this flux tube. All other power losses (P_{other}), e.g. due to viscous and compressional effects, only make a small contribution to P_{loss}. Finally, the total power flowing through the flux tube at the X-point position is also shown (P_{div}). It can be seen that there is no
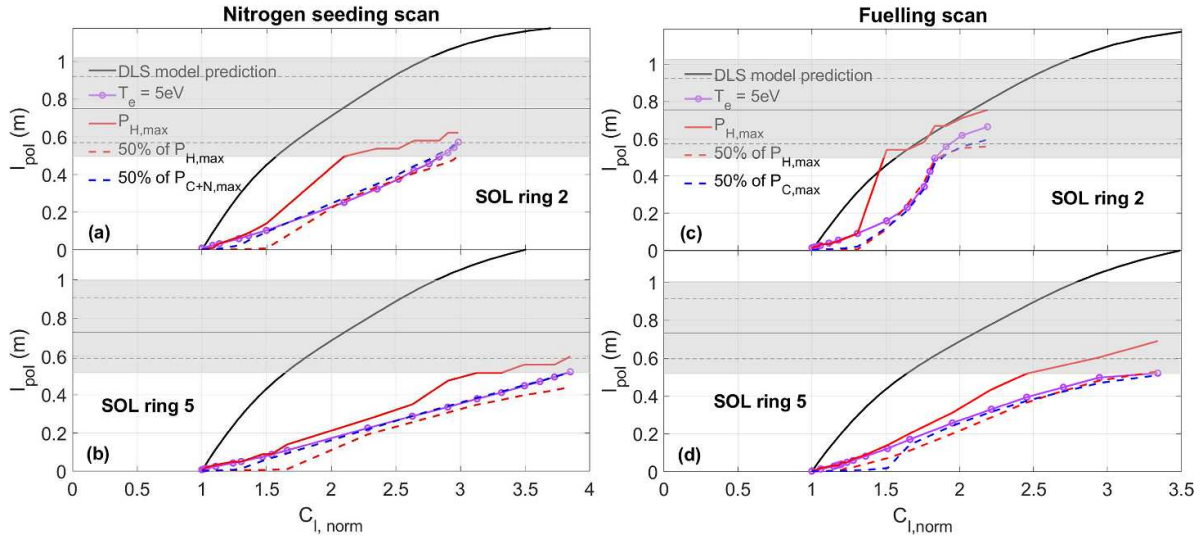
Figure 10. Detachment front location (multiple markers) in l_{pol} as a function of $C_{l,norm}$ as predicted by the DLS model and SOLPS. The region where $dB/dz > 50\%$ of the maximum dB/dz is shaded in grey.

change in the upstream power throughout the seeding scan. On the other hand, the upstream power reduces significantly in the fuelling scan. It appears that as the density is increased, the midplane profiles in the core region appear to evolve such that the power entering the low field side SOL reduces and the difference goes into the high field side SOL in these cases. It is not clear at this stage if this redistribution of the input power is physical, but it does not change the overall result in this paper.

4.2. Relationship between dB/dz and movement in l_{pol}

Since the original DLS model [23] predicted the movement of the detachment front along z, until now we have used the same z coordinate. However, as a practical matter for detachment control and divertor physics studies, we are interested in the detachment location in l_{pol}, the poloidal distance along the flux tube of interest. This is because: (a) diagnostic measurements of the detachment location and radiation profiles typically are made in the poloidal plane; (b) the radiation profile in poloidal space plays a central role in determining heat loads on the divertor PFCs and therefore a useful input for divertor design and/or optimisation; (c) the location of the detachment and thermal front with respect to the core plasma (X-point) will be useful in studying the impact of the extent of detachment on the core plasma (impurity levels, confinement, etc); and (d) it is much easier to visualize what is happening in the 2D poloidal cross-section.

To review the detachment front movement in the poloidal cross-section, we map the model predictions shown in figure 8 from z to l_{pol} using equation (1). The region of high dB/dz is also mapped to l_{pol}, shown in grey. The movement of the various markers in l_{pol} as a function of $C_{l,norm}$ is compared with the corresponding model prediction in figure 10. Similar to what was shown previously in z space, a reduction in sensitivity of the l_{pol} location of $P_{H,max}$ (and also $P_{C+N,max}$ or $P_{C,max}$, not shown) to changes in $C_{l,norm}$, though reduced, is observed in

the region of high dB/dz in both scans; that again indicates that the movement of the *thermal front region*, which is ahead of the detachment front, has indeed slowed down as a function of increasing $C_{l,norm}$. In the seeding scan, there are differences in the movement of 5 eV and 50% of $P_{H,max}$ points in l_{pol} space between figures 3 and 10. Our initial observation (figure 3) showed that at or before the high dB/dz region, these points clearly slowed down *as a function of the seeding rate*. We note that this is not observed for these points at or before the high dB/dz region *as a function of $C_{l,norm}$*. This difference could be partly due to variation in the thermal front width. Another likely reason is the fact that as the seeding rate is increased in equal steps, the steps in $C_{l,norm}$, dominated by f_{eff}, become smaller—this can be seen figure 6.

While the region of high dB/dz occupies only 15%–20% of the space between X-point and target in z, it occupies ≈40% of this space in l_{pol}. This is expected because the Super-X geometry essentially depends on the $1/R$ dependence of the toroidal field to achieve a high total flux expansion at the target. Figure 11(*a*) shows the total field, B, and the toroidal and poloidal components, B_{tor} and B_{pol}, between the X-point and target as a function of the major radius R for SOL ring 2. It can be seen that B_{tor} is the dominant component: the B profile mostly lies on top of the B_{tor} profile. Since $B_{tor} \propto 1/R$, in a scenario where $B \approx B_{tor}$, parallel gradients in B would exist mainly when the R coordinate of the field line increases going from X-point to the target, which also contributes to a change in l_{pol}. A 'faster' change in the R coordinate of B would increase dB/dz, but also simultaneously increase l_{pol}. This is visualised in figure 11(*b*) which displays the z coordinate of SOL ring 2 as a function of the l_{pol} coordinate. The regions of high parallel gradient in B are also highlighted (pink) for both z and l_{pol}. Basically, a significant chunk of l_{pol} is covered in 'moving' the field line to larger R to give rise to the region of 'high' dB/dz over a relatively small z range. However, this means that the significant reduction in detachment location sensitivity predicted by the model in z space translates to a
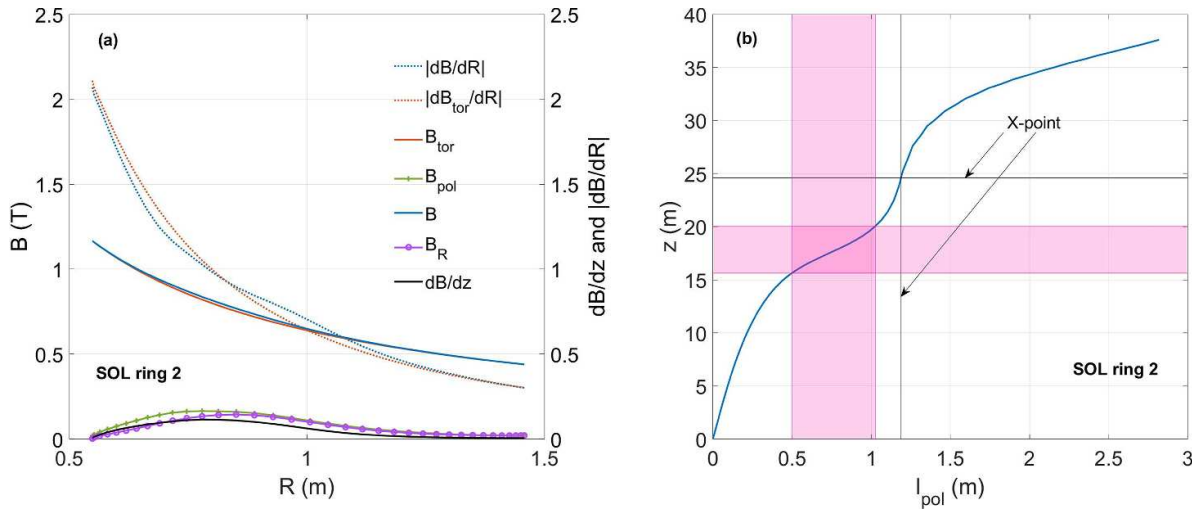
Figure 11. (*a*) Left *y*-axis: total magnetic field, *B*, toroidal and poloidal components, B_{tor} and B_{pol}, and major radial component of poloidal field, B_R, shown between X-point and target as a function of the major radius *R*; right *y*-axis: dB/dz, $|dB/dR|$ and $|dB_{tor}/dR|$ as a function of *R*. (*b*) The scaled (DLS) parallel distance from the target along the flux tube, *z*, as a function of the poloidal distance from the target, l_{pol}. Regions of 'high' dB/dz highlighted in pink.

mild reduction in detachment location sensitivity in l_{pol} in this geometry.

It is useful to discuss the implications of the fact that dB/dz is significantly smaller than $|dB/dR|$ (or $|dB_{tor}/dR|$), also displayed in figure 11(*a*). What 'moves' the field line to larger *R* going from the X-point to the target is the major radial component of B_{pol}, B_R (also shown in figure 11(*a*)). It seems that there is potentially scope for the Super-X geometry to be further optimised for slowing the front by increasing the peak in B_R at its present peak location in *R*, around 0.75 m; that would require larger coils currents. If possible, it could effectively increasing the maximum in dB/dz, which is likely to be of interest for improved control of the detachment/thermal front. However, increasing the peak in B_R will tend to reduce the parallel connection length, which could make detachment less accessible. It seems that there may be some trade off between front controllability once detached, and having the front off the target in the first place. Future work could focus on the efficacy of such an optimisation of the current MAST-U Super-X geometry.

On the other hand, it is interesting to note that $|dB/dR|$ is highest close to the X-point, where B_{pol} is naturally going to be low, and so significantly increasing B_R, compared to B_{tot} is not really possible. Further, the goal of achieving a higher dB/dz with a high B_R to move the field out faster in *R*, diminishes at larger *R*. These competing effects suggest that there is limited flexibility when it comes to changing or optimising the *location* of the high dB/dz region in the poloidal plane in this specific (MAST-U) divertor chamber geometry—one could argue that it is already optimized.

4.3. Variation in the thermal front width

The detachment front is essentially the cold end of the thermal front, the movement of which we have primarily focussed on.

The DLS model assumes that the thermal front is short compared to the length of the flux tube in the divertor. This means that the distance between the hot (z_h) and the cold end of the thermal front (at z_c) is small compared to distance (in *z*) between the target and X-point; this allows for thermal front (and detachment front) movement within the divertor—the goal of the model. In our analysis, z_c corresponds to the detachment front location and to the 50% point on the divertor side of the radiation profile. Without a clear idea of how to determine the hot end of the thermal front, z_h, we have chosen to track the points where the hydrogenic and impurity radiation losses fall to 50% of the maximum on the X-point side. In the simulations studied here, we find that the thermal front width varies in both scans as the injection rate is increased and can be comparable to the divertor size.

As was shown earlier in the paper, z_c moves from the target to a point where $dB/dz \approx 50\%$–90% of the maximum dB/dz in the flux tubes considered (figure 8). We find that the z_h markers we have chosen to track are already far into the region of $dB/dz \geqslant 50\%$ of the peak value soon after detachment onset and do not move much throughout both scans—this is shown in figure 12 for impurity radiation as well as hydrogenic losses. Most of the changes in the thermal front appear to be in its width in l_{pol} (and *z* and *l*) which shortens because of the movement of z_c during the two scans. As a result, it is difficult to develop a consistent SOLPS measure of the actual thermal front location in these simulations. We therefore track the location of the cold end of the thermal front or the detachment front as it is easier to define and its location and movement is co-related with that of the thermal front. However, this kind of variation in the thermal front width is likely an important reason for the observed quantitative disagreement.

Why is it that the thermal front becomes narrower as detachment proceeds? As discussed in the DLS model paper
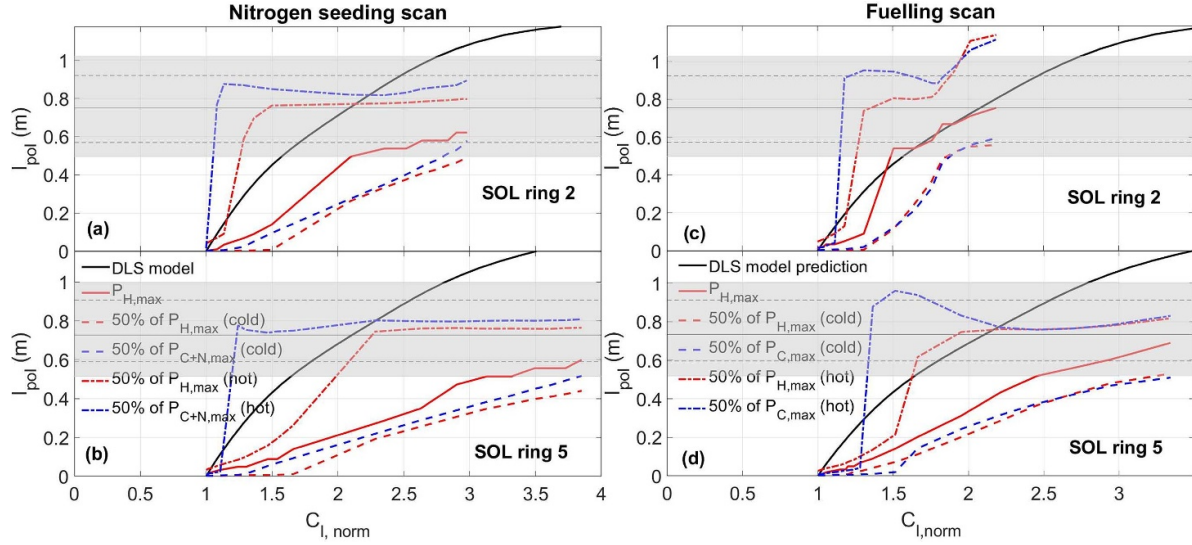
Figure 12. Comparison of the l_{pol} position of the SOLPS derived z_h markers, 50% of $P_{H,\max}$ (hot) and 50% of $P_{C/C+N,\max}$ (hot), and previously discussed z_c markers, 50% of $P_{H,\max}$ (cold) and 50% of $P_{C/C+N,\max}$ (cold), as a function of $C_{l,\mathrm{norm}}$. Location of the peak in hydrogenic power losses, $P_{H,\max}$, is also shown for reference.

[23], the length of the thermal front, between the 'hot' and 'cold' ends, Δ_{z_f}, is inversely proportional to $q_{||}$:

$$\Delta_{z_f} \equiv z_h - z_c \propto \frac{B_\times}{B(z_h)|q_{||}|}. \tag{15}$$

We can examine the changes in thermal front width in z for the case of an upstream density or impurity seeding scan, with a constant P_{SOL}: the thermal front width is largest at the detachment threshold as the total magnetic field is lowest ($q_{||}$ is lowest) near the target. As the detachment front moves in z towards the X-point, the thermal front width along z decreases as the magnitude of B in the front increases; As the front moves upstream, $B(z_h)$ and $q_{||}$ both increase, lowering Δ_{z_f}.

In the case of reactors using seeding of impurities for divertor radiation, Δ_{z_f} with respect to the divertor size of a reactor should be much smaller than that for MAST-U primarily because the $q_{||}$ entering the divertor is much larger than MAST-U ($\approx 1000\times$) and the divertor should be larger than that of MAST-U. However, if a reactor uses several radiators from low-Z to mid-Z which radiate over a wider temperature range, then this could lead to a broader thermal front than for a single low-Z impurity. Further work is required to quantify the dependency of the thermal front width on P_{div} and on the use of different impurities because a 'narrow thermal front' is an important DLS model assumption.

4.4. The causes of differences between the DLS model and SOLPS results

At first glance the quantitative mismatch between the DLS model and the SOLPS results is somewhat discouraging, in terms of justifying the predictive application of the DLS model. However, it at least argues that for the MAST-U Super-X divertor, the detachment location according to

SOLPS-ITER will be more controllable than predictions of the DLS model.

The quantitative mismatch between the DLS model prediction and the SOLPS results could be due to several factors, or some combination of: (a) As discussed regarding figure 9, there are several physics processes not included in the DLS model (mainly cross-field transport) that significantly affect the power balance; (b) the DLS model is a better predictor of a 'narrower' thermal front; or (c) interaction of the plasma with various surfaces that form the divertor region could have a local effect on the plasma, where recycling is raised or lowered as the detached or attached regions shift; and (d) the region of high $\mathrm{d}B/\mathrm{d}z$ coincides with the baffle/divertor entrance—in order to maintain plasma-neutral pressure balance, a tightly baffled divertor could potentially prevent the thermal front from moving into the main chamber.

4.4.1. Cross-field transport. In terms of case (a), more energy loss mechanisms could be added to the prediction as we have done with the use of f_{eff}. In particular, the cross-field losses, in most cases plotted in figure 9, *drop* during the seeding and fuelling scans, which is equivalent to an increasing P_{SOL} or decreasing f_{eff}. The net effect would be to reduce $C_{l,\mathrm{norm}}$ for the same z or l_{pol}, shifting the data closer to the DLS model prediction. However, such efforts to add more physics to the DLS model would degrade its clarity and usefulness. One could alternatively potentially 'compensate' for the missing physics in an ad hoc way by reducing the exponents of the three control variables—while that might work for a specific experimental case, it may not work generally.

4.4.2. Variation in the thermal front width. Case (b) has been addressed obliquely at points in the paper by assuming that the radiation profile extent is in rough correspondence to the thermal front—the 50% points on the leading and trailing sides

of the radiation profile approximating z_h and z_c respectively, with the peak in radiation being somewhere in the middle of the thermal front. We have shown that the peak in the radiation profile is closer to the DLS prediction than the detachment front in either l_{pol} or z space. z_h hardly moves after detachment, staying in the high dB/dz region, past the peak.

4.4.3. Neutral trapping and associated power loss. There are already existing studies that address case (c): experimental and modelling studies of DIII-D [48], TCV [49] and MAST-U [50] show that neutral recycling and location of baffles can work to either enhance (DIII-D, MAST-U) or reduce (TCV) the effect of total flux expansion. The effect is thought to be due to increasing or decreasing the neutral ionization in the divertor (or more specifically, due changes in 'neutral trapping' [49]), raising the target density and lowering the target temperature through modification of power losses in the flux tube.

4.4.4. The role of a tight baffle and plasma-neutral pressure balance. In this MAST-U study, the role of the baffle at the entrance to the divertor could be affecting the movement of the detachment front. We find that the detachment front at the highest seeding/fuelling rates is located $\sim$15–20 cm downstream in l_{pol} from the N seeding location on the 'roof' of the divertor chamber (figures 2(*a*) and (*b*)); beyond that the curved section of the baffle forms the entrance to the divertor. In such a tightly baffled divertor as exists in MAST-U, the baffle strongly limits the capability of neutrals to move along the side of the plasma, which itself serves to ionize most, if not all, neutrals trying cross through it to escape into the main chamber. Neutrals trying to penetrate that region are ionized, flow back to the targets and recycle as neutrals again. The detachment front then sits slightly inside the entrance to the divertor, in a region of high neutral gas pressure. If the detachment front were to move past the divertor entrance towards the X-point, then the narrow entrance to the divertor is no longer as well plugged by the plasma, and the neutral gas pressure behind and in the thermal front could drop. The need to maintain pressure balance between the plasma and the neutrals could cause the front to move back into the divertor—we speculate that this could provide a feedback mechanism which would help prevent the detachment front from leaving the closed divertor. This physics associated with plasma-neutral pressure balance, which is not included in the DLS model, would be captured in SOLPS. Based on the analysis in [24], it appears that allowing for pressure variation along the flux tube has the biggest impact on the DLS model predictions of detachment threshold, and would likely also affect the detachment window. This aspect therefore needs further investigation.

5. Conclusions and summary

Detachment evolution in the MAST-U Super-X geometry has been studied using the SOLPS-ITER code, with a focus on the

sensitivity of the detachment front location to control parameters. Two sets of steady state solutions were obtained by scanning the D_2 and N injections rates at fixed input power (2.5 MW), ranging from attached to strongly detached conditions. Movement of the detachment front location is tracked in two characteristic flux tubes as a function of physics control parameters: power passing through the flux tube at the X-point position (P_{div}), upstream density (n_u) and impurity fraction (f_I). Different measures of the detachment location are developed and compared for tracking its location.

In both seeding and fuelling scans, the detachment front location initially moves quickly off the target along a field line or equivalently in the poloidal direction for equal steps of N seeding or D_2 fuelling. The front movement slows down as it moves through a region of increasing dB/dz. After a factor of up to $10\times$ and $5\times$ increase in the seeding and fuelling rates past the detachment threshold, the detachment front has reached less than halfway to the X-point in l_{pol} where $dB/dz \sim$50% of its maximum value, close to the baffle or divertor entrance.

The SOLPS results are compared to the predictions of the DLS model which is based only on energy balance and makes a number of simplifying assumptions to ease understanding and predict dependencies on various divertor design characteristics. Both the DLS model and SOLPS predict a reduction in the sensitivity of the detachment front location along a field line, z, to control parameters in the region of high dB/dz for the MAST-U Super-X configuration. Such a drop in sensitivity to controls is equivalent to enhanced detachment control. Both the DLS model and the SOLPS cases studied suggest that the MAST-U Super-X configuration may be able to accommodate larger power transients compared to a conventional divertor while still keeping the divertor plasma detached with the detachment front kept away from the X-point or target. This is because of the relative large change in controls required to move the thermal/detachment front through a region of high parallel gradients in B.

There is a quantitative mismatch between SOLPS and DLS model predictions of the detachment front location sensitivity to control parameter variation—for a given change in $C_{l,norm}$, the DLS model predicts faster movement of the detachment front towards the X-point (detachment location more 'sensitive' to control parameter variation) compared to SOLPS results. This could be due to a number of reasons: for example, the DLS model does not include cross-field transport of power out of the flux tube and the thermal front width is assumed to be small compared to the divertor size. Such shortcomings may be less important when the model is applied to reactor-level parallel heat fluxes where the thermal front length in z, for a single low-Z impurity seeded scenario, may be shorter than for MAST-U. However, if a combination of low-Z and mid-Z impurities are seeded, this could increase the thermal front width. Further work is needed to understand the dependence of the thermal front width on the power entering the divertor and the impurity (or impurities) chosen to dissipate that power.

The extent of the high dB/dz region is changed when examined in l_{pol} compared to along a field line (z space). The high dB/dz region in z space is small, $\sim$15%–20% of the distance from target to X-point. In comparison, the high dB/dz region in l_{pol} space is a much larger ($\sim$40%) fraction of the distance from the target to the X-point. That translates to a milder reduction in sensitivity in poloidal space for the divertor geometry considered. It appears that there is limited flexibility when it comes to changing or optimising the location of the region of high parallel gradients in B in the poloidal plane of MAST-U. However, there may be scope to further optimise the Super-X geometry used here: the maximum parallel gradient in B in its existing location could be increased further if increasing the poloidal field (B_{pol}), lowering the poloidal flux expansion, is possible. However, that needs further study.

Furthermore, the location and effect of surfaces could be important. For example, the region where the detachment front becomes less sensitive to changes in control variables is also close the divertor opening. It has already been shown that the baffle has a significant impact on the access to detachment [27]. It is possible that maintaining plasma-neutral pressure balance in a tightly baffled divertor could also be contributing to the reduction in the front location sensitivity to controls, in addition the parallel gradients in B. Thus, the trapping of neutrals in the divertor, which can change as the detachment moves, could also be playing a role in slowing down the detachment front location movement, but this requires further investigation. If the tight baffling indeed plays a role in slowing down the front, it naturally gives rise to the question of which effect is playing the dominant role, and motivates future work to disentangle the relative contributions of these two effects.

Acknowledgments

Appendix. Comparison of linear and non-linear DLS model predictions

The 'linear' and 'non-linear' (real B-field) DLS model predictions can be understood better by studying equation (5), reproduced below:

$$
\begin{aligned}
C_{l,\mathrm{norm}}(z_f) &= \frac{B_f \times \left[\int_{z_f}^{z_\times} B^2(z)\mathrm{d}z + \int_{z_\times}^{L} \frac{B^2(z)(L-z)}{L-z_\times}\mathrm{d}z\right]^{-2/7}}{B_t \times \left[\int_{z_t}^{z_\times} B^2(z)\mathrm{d}z + \int_{z_\times}^{L} \frac{B^2(z)(L-z)}{L-z_\times}\mathrm{d}z\right]^{-2/7}} \\
&= \frac{B_f}{B_t} \times \left(\frac{B_{\mathrm{INT},f}}{B_{\mathrm{INT},t}}\right)^{-2/7}.
\end{aligned} \tag{A.1}
$$

According to the model, $C_{l,\mathrm{norm}}$ is essentially a product of two ratios: the ratio of the magnitude of B at the front location to that at the target, and ratio of the integrals in the square brackets which we have called $B_{\mathrm{INT},t}$ for when the front is at the target and $B_{\mathrm{INT},f}$ for when the front is somewhere between the target and X-point (as shown in equation (A.1)).

We utilise figures A.13 and A.14 to take a closer look at the DLS model. Figure A.13 shows a comparison of total magnetic field from SOL ring 2 of our SOLPS simulation (blue) and the magnetic field assumed to obtain the linear DLS prediction shown in figure 8 (yellow). For contrast to the linear field optimised for a $B_\times/B_t$ similar to that in a conventional divertor, we have also looked at the DLS model prediction assuming linear variation in B, but with a $B_\times/B_t$ equal to that in our SOLPS simulation (red). Figure A.14(*a*) shows the DLS predictions of $C_{l,\mathrm{norm}}$ for the $B(z)$ profiles shown in figures A.13 and A.14(*b*) shows the corresponding components of $C_{l,\mathrm{norm}}$ (the two aforementioned ratios that $C_{l,\mathrm{norm}}$ is composed of).

In the following we make a case that the strong increase in $C_{l,\mathrm{norm}}$ between 15 m–20 m in the non-linear case is mainly driven by the increase in B_f (i.e. the ratio B_f/B_t) in that region. The ratio of the integrals does not play a significant role in this region. In the case where linear variation in B is assumed, the reduction in sensitivity of z_f to $C_{l,\mathrm{norm}}$ (even though dB/dz is constant between the target and X-point) is a result of a nonlinear increase in the ratio $(B_{\mathrm{INT},f}/B_{\mathrm{INT},t})^{-2/7}$ (due to the drop in connection length), which makes the dominant contribution to $C_{l,\mathrm{norm}}$ in the case where $B_t = 1$. The contribution of the ratio B_f/B_t to $C_{l,\mathrm{norm}}$ is small in the case where $B_t = 1$, but dominant in the linear case where $B_\times/B_t$ is the same as that in the non-linear case. It is interesting to note that the overall change in $C_{l,\mathrm{norm}}$ predicted by the generalised (non-linear) DLS model is similar to the linear case with the same $B_\times/B_t$, similar to what was found in [24]. In other words, the size of the detachment window depends primarily on the B-field strength at the X-point and target ends of the flux tube, rather than the path that the flux tube takes in the divertor. The generalised DLS model, however, is required to be able to predict *where* one can expect a reduction in the detachment location sensitivity to controls between the X-point and target. This comparison highlights the fact that in the end, according to the DLS model a large $B_\times/B_t$ and dB/dz are required to significantly reduce the detachment location sensitivity to controls.
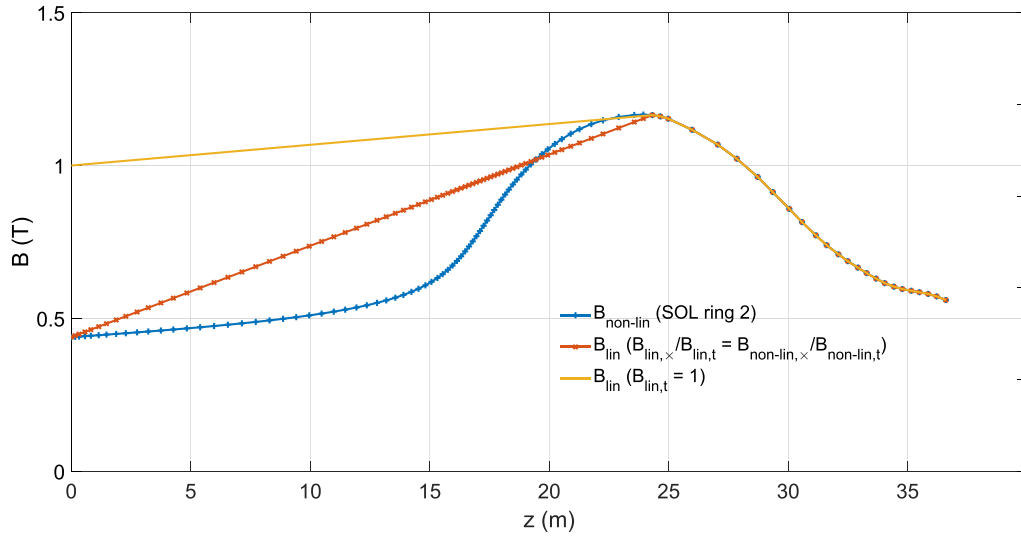
Figure A.13. Total magnetic field from SOLPS simulations for SOL ring 2 ($B_{non-lin}$, blue), linear variation in total magnetic field between X-point and target with $B_t = 1$ (yellow) and linear variation in total magnetic field between X-point and target with $B_\times/B_t$ same as SOLPS simulation (red).
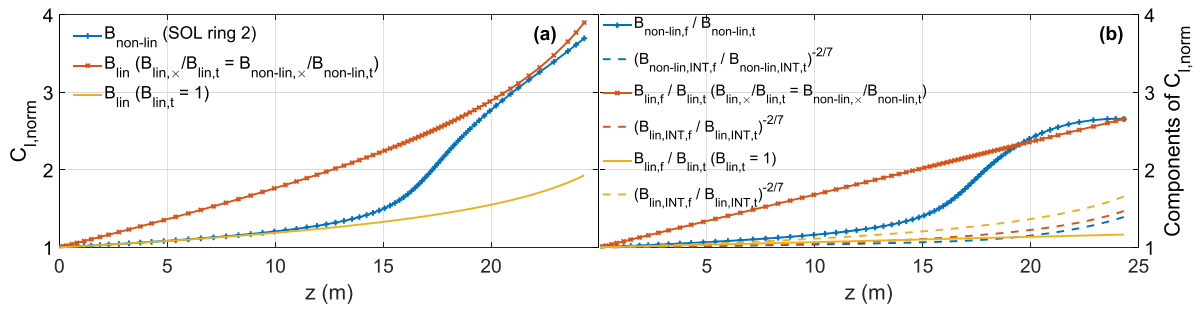

Figure A.14. Components of $C_{l,\text{norm}}$ as a function of z obtained from the SOLPS geometry (*a*) and assuming linear variation in B (*b*). The linear B variation assumed and that from the SOLPS geometry are also shown for comparison.

ORCID iDs

O. Myatra ![ORCID] https://orcid.org/0000-0002-1469-2429
B. Lipschultz ![ORCID] https://orcid.org/0000-0001-5968-3684
K. Verhaegh ![ORCID] https://orcid.org/0000-0002-0500-2764
B. Dudson ![ORCID] https://orcid.org/0000-0002-0094-4867

References

[1] Loarte A. *et al* 2007 Chapter 4: power and particle control *Nucl. Fusion* **47** S203
[2] Federici G. *et al* 2001 Plasma-material interactions in current tokamaks and their implications for next step fusion reactors *Nucl. Fusion* **41** 1967–2137
[3] Stangeby P.C. 1993 Can detached divertor plasmas be explained as self-sustained gas targets? *Nucl. Fusion* **33** 1695–705
[4] Pitcher C.S. and Stangeby P.C. 1997 Experimental divertor physics *Plasma Phys. Control. Fusion* **39** 779
[5] Stangeby P.C. 2000 *The Plasma Boundary of Magnetic Fusion Devices* (IOP Publishing)
[6] Lipschultz B., LaBombard B., Terry J.L., Boswell C. and Hutchinson I.H. 2007 Divertor physics research on Alcator C-Mod *Fusion Sci. Technol.* **51** 369–89
[7] Kallenbach A. *et al* (The ASDEX Upgrade Team) 2013 Impurity seeding for tokamak power exhaust: from present devices via ITER to DEMO *Plasma Phys. Control. Fusion* **55** 124041
[8] Lumma D., Terry J.L. and Lipschultz B. 1997 Radiative and three-body recombination in the Alcator C-Mod divertor *Phys. Plasmas* **4** 2555–66
[9] Lipschultz B., Goetz J.A., LaBombard B., McCracken G.M., Ohkawa H., Takase Y. and Terry J.L. 1997 Modification and control of divertor detachment in Alcator C-Mod *J. Nucl. Mater.* **241–243** 771–6
[10] Pitcher C.S., Carlson A.W., Fuchs C., Herrmann A., Suttrop W., Schweinzer J. and Weinlich M. (ASDEX Upgrade Teama and NBI Group) 1997 Routes to divertor detachment in ASDEX upgrade *J. Nucl. Mater.* **241–243** 696–700
[11] Verhaegh K. *et al* 2019 An improved understanding of the roles of atomic processes and power balance in divertor target ion current loss during detachment *Nucl. Fusion* **59** 126038
[12] Smolders A. *et al* (The TCV Team) 2020 Comparison of high density and nitrogen seeded detachment using SOLPS-ITER simulations of the tokamak á configuration variable *Plasma Phys. Control. Fusion* **62** 125006
[13] Hutchinson I. 1994 Thermal front analysis of detached divertors and marfes *Nucl. Fusion* **34** 1337–48

[14] Goetz J.A. *et al* 1996 Comparison of detached and radiative divertor operation in Alcator C-Mod *Phys. Plasmas* **3** 1908–15

[15] Harrison J.R. *et al* 2017 Detachment evolution on the TCV tokamak *Nucl. Mater. Energy* **12** 1071–6

[16] Kallenbach A. *et al* 2015 Partial detachment of high power discharges in ASDEX upgrade *Nucl. Fusion* **55** 053026

[17] Mccracken G.M., Lipschultz B., Labombard B., Goetz J.A., Granetz R.S., Jablonski D., Lisgo S., Ohkawa H., Stangeby P.C. and Terry J.L. 1997 Impurity screening in ohmic and high confinement (h-mode) plasmas in the Alcator C-Mod tokamak *Phys. Plasmas* **4** 1681–9

[18] The JET Team 1995 Highly radiating and detached plasmas on carbon and beryllium targets *Plasma Phys. Control. Fusion* **37** A227

[19] Goetz J.A., Lipschultz B., Pitcher C.S., Terry J.L., Bonoli P.T., Rice J.E. and Wukitch S.J. 1999 Impurity compression and enrichment studies on Alcator C-Mod *J. Nucl. Mater.* **266** 354–9

[20] Bosch H.-S., Ullrich W., Coster D., Gruber O., Haas G., Neuhauser J., Schneider R. and Wolf R. 2001 Helium transport and exhaust with an ITER-like divertor in ASDEX upgrade *J. Nucl. Mater.* **290-293** 836–9

[21] Kallenbach A. *et al* 2010 Divertor power load feedback with nitrogen seeding in ASDEX upgrade *Plasma Phys. Control. Fusion* **52** 055002

[22] Kallenbach A., Bernert M., Eich T., Fuchs J., Giannone L., Herrmann A., Schweinzer J. and Treutterer W. 2012 Optimized tokamak power exhaust with double radiative feedback in ASDEX upgrade *Nucl. Fusion* **52** 122003

[23] Lipschultz B., Parra F.I. and Hutchinson I.H. 2016 Sensitivity of detachment extent to magnetic configuration and external parameters *Nucl. Fusion* **56** 056007

[24] Cowley C., Lipschultz B., Moulton D. and Dudson B. 2022 Optimizing detachment control using the magnetic configuration of divertors *Nucl. Fusion* **62** 086046

[25] Stork D., Meyer H., Akers R., Buttery R., Chapman I., Conway N., Cowley S., Cunningham G., Davis S. and Field A. 2010 The upgrade to the mega amp spherical tokamak (available at: https://inis.iaea.org/search/search. aspx?orig_q=RN:43043465)

[26] Morris A.W. 2012 Mast: results and upgrade activities *IEEE Trans. Plasma Sci.* **40** 682–91

[27] Havlíčková E., Harrison J., Lipschultz B., Fishpool G., Kirk A., Thornton A., Wischmeier M., Elmore S. and Allan S. 2015 Solps analysis of the MAST-U divertor with the effect of heating power and pumping on the access to detachment in the Super-X configuration *Plasma Phys. Control. Fusion* **57** 115001

[28] Schneider R., Bonnin X., Borrass K., Coster D.P., Kastelewicz H., Reiter D., Rozhansky V.A. and Braams B.J. 2006 Plasma edge physics with B2-eirene *Contrib. Plasma Phys.* **46** 3–191

[29] Moulton D., Lipschultz B. and Harrison J. 2017 Detachment onset in MAST-U according to SOLPS-ITER *44th EPS Conf. on Plasma Physics* (*Belfast, UK, 26–30 June 2017*) pp 1–45 (available at: http://ocs.ciemat.es/EPS2017PAP/ pdf/O5.129.pdf)

[30] Havlíčková E., Wischmeier M., Lipschultz B. and Fishpool G. 2015 The effect of the Super-X divertor of MAST upgrade on impurity radiation as modelled by SOLPS *J. Nucl. Mater.* **463** 1209–13

[31] Kirk A., Counsell G.F., Fundamenski W., Ahn J.-W., Taylor D., Walsh M.J. and Yang Y. (The MAST Team) 2004 A comparison of mid-plane scrape-off-layer measurements with model predictions in MAST and the calculation of cross-field transport coefficients *Plasma Phys. Control. Fusion* **46** 1591–603

[32] Harrison J.R., Fishpool G.M. and Kirk A. 2013 L-mode and inter-ELM divertor particle and heat flux width scaling on MAST *J. Nucl. Mater.* **438** S375–8

[33] Thornton A.J. and Kirk A. 2014 Scaling of the scrape-off layer width during inter-ELM H modes on MAST as measured by infrared thermography *Plasma Phys. Control. Fusion* **56** 055008

[34] Eich T. *et al* 2013 Scaling of the tokamak near the scrape-off layer H-mode power width and implications for ITER *Nucl. Fusion* **53** 093031

[35] Theiler C. *et al* 2017 Results from recent detachment experiments in alternative divertor configurations on TCV *Nucl. Fusion* **57** 072008

[36] Ravensbergen T. *et al* (The EUROfusion MST1 Team) 2020 Development of a real-time algorithm for detection of the divertor detachment radiation front using multi-spectral imaging *Nucl. Fusion* **60** 066017

[37] Leonard A.W., Mahdavi M.A., Lasnier C.J., Petrie T.W. and Stangeby P.C. 2012 Scaling radiative divertor solutions to high power in DIII-D *Nucl. Fusion* **52** 063015

[38] Reiter D. 2011 The data file AMJUEL: additional atomic and molecular data for EIRENE (available at: www. researchgate.net/publication/228728483_The_data_file_ AMJUEL_Additional_atomic_and_molecular_data_for_ EIRENE)

[39] Lengyel L. 1981 Analysis of radiating plasma boundary layers (available at: https://inis.iaea.org/search/search.aspx?orig_ q=RN:13657893)

[40] Lackner K. and Schneider R. 1993 The role of edge physics and confinement issues in the fusion reactor *Fusion Eng. Des.* **22** 107–16

[41] Post D., Putvinskaya N., Perkins F.W. and Nevins W. 1995 Analytic criteria for power exhaust in divertors due to impurity radiation *J. Nucl. Mater.* **220-222** 1014–8

[42] Reinke M. 2017 Heat flux mitigation by impurity seeding in high-field tokamaks *Nucl. Fusion* **57** 034004

[43] Goldston R.J., Reinke M.L. and Schwartz J.A. 2017 A new scaling for divertor detachment *Plasma Phys. Control. Fusion* **59** 055015

[44] Post D.E., Jensen R.V., Tarter C.B., Grasberger W.H. and Lokke W.A. 1977 Steady-state radiative cooling rates for low-density, high-temperature plasmas *At. Data Nucl. Data Tables* **20** 397–439

[45] Moulton D., Stangeby P.C., Bonnin X. and Pitts R.A. 2021 Comparison between SOLPS-4.3 and the lengyel model for ITER baseline neon-seeded plasmas *Nucl. Fusion* **61** 046029

[46] Jaervinen A.E., Allen S.L., Leonard A.W., McLean A.G., Moser A.L., Rognlien T.D. and Samuell C.M. 2020 Role of poloidal e × b drift in divertor heat transport in DIII-D *Contrib. Plasma Phys.* **60** e201900111

[47] Kotschenreuther M., Valanju P., Covele B. and Mahajan S. 2013 Magnetic geometry and physics of advanced divertors: the x-divertor and the snowflake *Phys. Plasmas* **20** 102507

[48] Petrie T.W. *et al* 2013 Effect of separatrix magnetic geometry on divertor behavior in DIII-D *J. Nucl. Mater.* **438** S166–9

[49] Fil A., Lipschultz B., Moulton D., Dudson B.D., Février O., Myatra O., Theiler C., Verhaegh K. and Wensing M. 2020 Separating the roles of magnetic topology and neutral trapping in modifying the detachment threshold for TCV *Plasma Phys. Control. Fusion* **62** 035008

[50] Fil A., Lipschultz B., Moulton D., Thornton A., Dudson B.D., Myatra O. and Verhaegh K. (The EUROfusion MST1 Team) 2022 Comparison between MAST-U conventional and Super-X configurations through SOLPS-ITER modelling *Nucl. Fusion* **62** 096026